

# 1 Nucleotide inhibition of the 2 pancreatic ATP-sensitive K<sup>+</sup> channel 3 explored with patch-clamp 4 fluorometry

5 **Samuel G. Usher<sup>1</sup>, Frances M. Ashcroft<sup>1\*</sup>, Michael C. Puljung<sup>1\*</sup>**

\*For correspondence:

[frances.ashcroft@dpag.ox.ac.uk](mailto:frances.ashcroft@dpag.ox.ac.uk)  
(FMA);  
[michael.puljung@dpag.ox.ac.uk](mailto:michael.puljung@dpag.ox.ac.uk)  
(MCP)

6 <sup>1</sup>Department of Physiology, Anatomy and Genetics, University of Oxford, Oxford OX1  
7 3PT, United Kingdom

8 **Abstract** Pancreatic ATP-sensitive K<sup>+</sup> channels (K<sub>ATP</sub>) comprise four inward rectifier subunits (Kir6.2), each associated with a sulphonylurea receptor (SUR1). ATP/ADP binding to Kir6.2 shuts K<sub>ATP</sub>. Mg-nucleotide binding to SUR1 stimulates K<sub>ATP</sub>. In the absence of Mg<sup>2+</sup>, SUR1 increases the apparent affinity for nucleotide inhibition at Kir6.2 by an unknown mechanism. We simultaneously measured channel currents and nucleotide binding to Kir6.2. Fits to combined data sets suggest that K<sub>ATP</sub> closes with only one nucleotide molecule bound. A Kir6.2 mutation (C166S) that increases channel activity did not affect nucleotide binding, but greatly perturbed the ability of bound nucleotide to inhibit K<sub>ATP</sub>. Mutations at position K205 in SUR1 affected both nucleotide affinity and the ability of bound nucleotide to inhibit K<sub>ATP</sub>. This suggests a dual role for SUR1 in K<sub>ATP</sub> inhibition, both in directly contributing to nucleotide binding and in stabilising the nucleotide-bound closed state.

## 21 **Introduction**

22 ATP-sensitive K<sup>+</sup> channels (K<sub>ATP</sub>) couple the metabolic state of a cell to its electrical activity (*Ashcroft*  
23 *and Rorsman, 2013*). In pancreatic β-cells, closure of K<sub>ATP</sub> in response to glucose uptake trig-  
24 gers insulin secretion. As such, mutations in K<sub>ATP</sub> that affect its response to changes in cellular  
25 metabolism cause diseases of insulin secretion, e.g. neonatal diabetes and persistent hyperinsu-  
26 linemic hypoglycaemia of infancy (PHHI; *Quan et al. (2011); Ashcroft et al. (2017)*). K<sub>ATP</sub> is com-  
27 posed of four inwardly rectifying K<sup>+</sup> channel subunits (Kir6.2 in pancreatic β-cells), which form the  
28 channel pore and four modulatory sulphonylurea receptor subunits (SUR1 in β-cells; Figure 1A;  
29 *Aguilar-Bryan et al. (1995); Inagaki et al. (1995); Sakura et al. (1995); Inagaki et al. (1997)*). SUR1  
30 is a member of the ABC transporter family but lacks any transport activity (*Aguilar-Bryan et al.*,

31     1995; *Tusnady et al., 1997*).  $K_{ATP}$  responds to metabolism via adenine nucleotide binding to three  
 32     distinct classes of intracellular nucleotide-binding site (one on each Kir6.2 subunit and two on each  
 33     SUR1 subunit—making twelve sites in total (*Vedovato et al., 2015*). Binding of ATP or ADP to Kir6.2  
 34     inhibits  $K_{ATP}$  channel activity (*Tucker et al., 1997; Proks et al., 2010*), whereas binding of nucleotides  
 35     to SUR1 stimulates  $K_{ATP}$  (*Nichols et al., 1996; Tucker et al., 1997*). The stimulatory activity of nu-  
 36     cleotides on  $K_{ATP}$  depends on  $Mg^{2+}$  (*Gribble et al., 1998*), whereas their inhibitory effect on Kir6.2  
 37     does not (*Tucker et al., 1997*).

38       In addition to nucleotide-dependent activation, SUR1 confers several other properties on the  
 39     Kir6.2. First, association with SUR1 increases the open probability ( $P_{open}$ ) of Kir6.2 (*Babenko and*  
 40     *Bryan, 2003; Chan et al., 2003; Fang et al., 2006*). Despite this increase in  $P_{open}$ , SUR1 also paradox-  
 41     ically increases the apparent affinity for nucleotide inhibition at Kir6.2 by an unknown mechanism  
 42     (*Tucker et al., 1997*). SUR1 is also responsible for high-affinity inhibition of  $K_{ATP}$  by antidiabetic  
 43     sulphonylureas and glinides as well as activation by  $K_{ATP}$ -specific  $K^+$  channel openers (*Tucker et al.,*  
 44     *1997*). Finally, SUR1 and Kir6.2 must co-assemble to ensure mutual exit from the endoplasmic retic-  
 45     ulum and correct trafficking to the plasma membrane (*Zerangue et al., 1999*).

46       To date, the primary means of studying nucleotide-dependent effects on  $K_{ATP}$  channel func-  
 47     tion has been with electrophysiological approaches, which measure the summed activity of all  
 48     three classes of binding site acting in concert. Thus, it can be difficult to separate the contribu-  
 49     tions of each class of site to the opening and closing of the channel pore and to properly distin-  
 50     guish between nucleotide binding and channel gating. To overcome these limitations, we have  
 51     applied a novel approach to directly measure nucleotide binding to each individual class of site in  
 52      $K_{ATP}$  (*Puljung et al., 2019*). This method utilizes Förster resonance energy transfer (FRET) between  
 53     channels labelled with the fluorescent unnatural amino acid 3-(6-acetylnaphthalen-2-ylamino)-2-  
 54     aminopropanoic acid (ANAP) and fluorescent trinitrophenyl (TNP) analogues of adenine nucleotides  
 55     (Figure 1B). As we show here, this method is readily combined with patch-clamp electrophysiology  
 56     so that nucleotide binding and regulation of current can be measured simultaneously. This has  
 57     enabled us to quantitatively assess nucleotide binding to Kir6.2 and explore how this is coupled to  
 58     channel inhibition in both wild-type  $K_{ATP}$  and  $K_{ATP}$  carrying mutations that impair ATP inhibition.

## 59     Results

60     **Measuring nucleotide binding to Kir6.2.** We previously used this FRET-based binding assay to  
 61     measure nucleotide binding to the second nucleotide-binding site of SUR1 (*Puljung et al., 2019*).  
 62     To measure binding to Kir6.2 in the complete  $K_{ATP}$  complex (four full-length Kir6.2 subunits co-  
 63     expressed with four full-length SUR1 subunits), we replaced a tryptophan at position 311 (W311)  
 64     that is 26 Å from the location of the inhibitory nucleotide-binding site on Kir6.2 with ANAP (Figure  
 65     1C) such that each subunit is labelled with one ANAP molecule. We designate this construct Kir6.2\*.  
 66     Based on the theoretical FRET efficiency calculated from the Förster equation and available cryo-  
 67     EM structures (*Martin et al., 2017, 2019*), we expect 91% FRET efficiency between ANAP at position  
 68     311 and a TNP-ATP molecule bound to Kir6.2, and only 4% FRET efficiency to TNP-ATP bound to  
 69     the closest nucleotide-binding site on SUR1 (nucleotide binding site 1, Figure 1D). We also expect  
 70     very little FRET between ANAP at position 311 and TNP-ATP bound to neighbouring Kir6.2 subunits

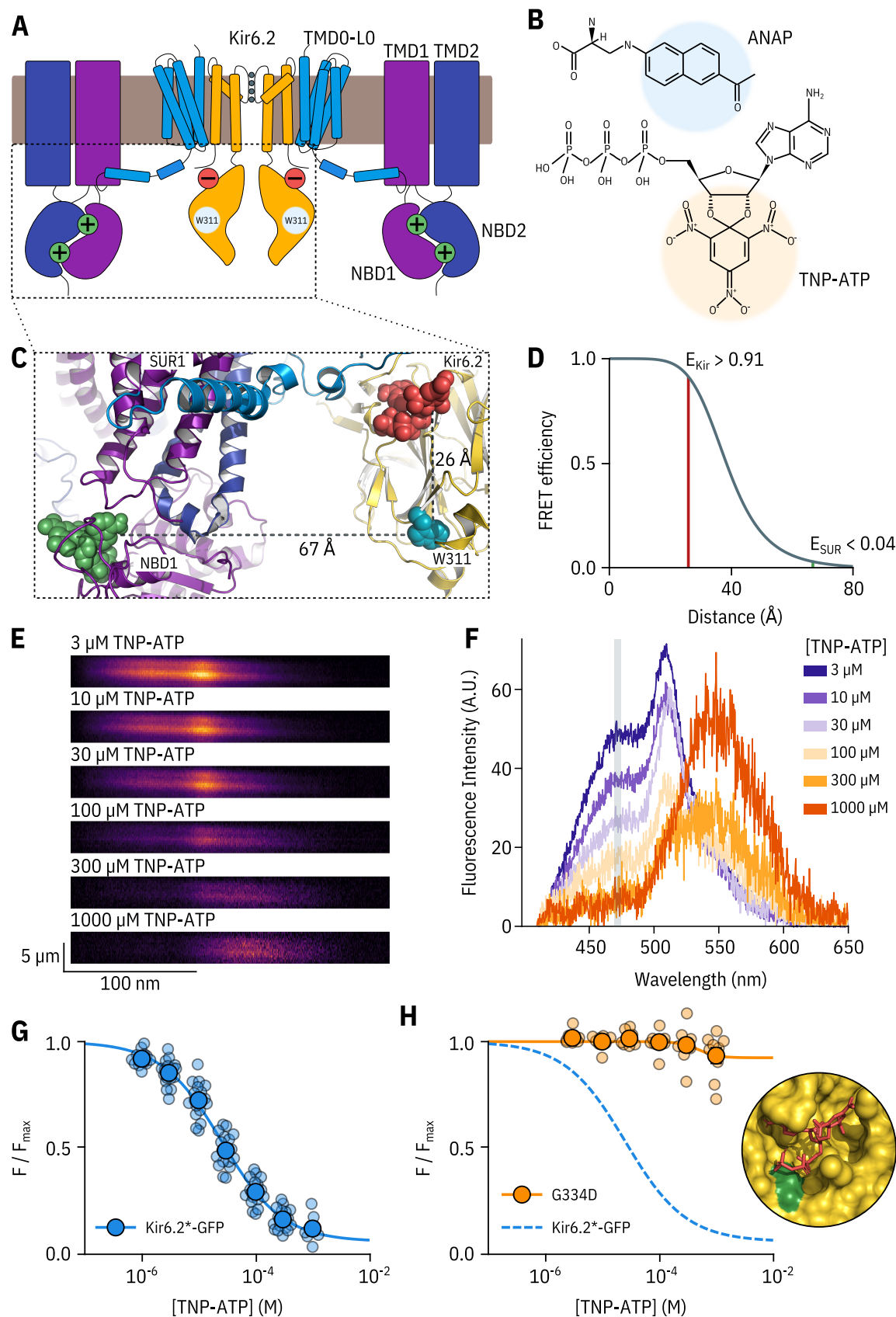


**Figure 1. A FRET assay to measure nucleotide binding to Kir6.2.**

**Figure 1. A FRET assay to measure nucleotide binding to Kir6.2.** **A.** Cartoon illustrating the topology of K<sub>ATP</sub>. The inhibitory nucleotide-binding site on Kir6.2 is shown in red; the stimulatory nucleotide-binding sites on SUR1 are shown in green. The three transmembrane domains of SUR1 are designated TMD0, TMD1, and TMD2. The loop connecting TMD0 to TMD1 is designated L0. The nucleotide binding domains of SUR1 are labelled NBD1 and NBD2. **B.** Chemical structures of ANAP and TNP-ATP. The fluorescent moieties are highlighted. **C.** Side view of the structure of the cytosolic domains of Kir6.2 (PDB accession #6BAA) and one SUR1 subunit (PDB accession #6PZI). TNP-ATP (red, from PDB accession #5XW6) was docked into the nucleotide-binding site of Kir6.2 and positioned in NBS1 of SUR1 (green, from PDB accession #3AR7) by alignment as described in Materials and Methods. Distances from the native tryptophan at position 311 in Kir6.2 to the fluorescent moieties of the TNP-ATPs are displayed in Å. **D.** Theoretical FRET efficiency between ANAP and TNP-ATP as a function of distance, calculated from the Förster equation. The distances and corresponding FRET efficiencies between ANAP at position 311 and TNP-ATP bound to Kir6.2 (E<sub>Kir</sub>) and SUR1 (E<sub>SUR</sub>) are indicated. **E.** Spectral images acquired from an unroofed membrane expressing Kir6.2\*-GFP + SUR1 and exposed to increasing concentrations of TNP-ATP. The y-dimension in each image represents distance. The x-dimension represents wavelength. **F.** Line-averaged, background-subtracted spectra from **E** displayed with increasing concentrations of TNP-ATP coloured from purple to orange. The three fluorophores have distinct peaks: ANAP at 472 nm, GFP at 508 nm, and TNP-ATP at 561 nm. The shaded rectangle indicates the wavelength range used to measure ANAP intensity. **G.** Concentration-response relationship for binding of TNP-ATP to Kir6.2\*-GFP + SUR1 in unroofed membranes. Data were plotted as  $F/F_{max}$ , where  $F_{max}$  is the fluorescence intensity in the absence of nucleotide. The smooth curve is a descriptive Hill fit.  $EC_{50} = 25.6 \mu\text{M}$ ,  $h = 0.82$ ,  $E_{max} = 0.93$ ,  $n = 18$ . **H.** Concentration-response relationship for binding of TNP-ATP to Kir6.2\*-G334D-GFP + SUR1 in unroofed membranes. The dashed blue curve is the fit from **G**. The orange curve is a descriptive Hill fit to the G334D data.  $EC_{50} = 493 \mu\text{M}$ ,  $h = 2.63$ ,  $E_{max} = 0.08$ ,  $n = 9$ . The inset shows the location of G334D (green) in relation to the inhibitory ATP binding site on Kir6.2 (PDB accession #6BAA). TNP-ATP (PDB accession #5XW6) shown in red sticks.

**Figure 1 – figure supplement 1. ANAP labelling is specific and only full-length Kir6.2 is expressed at the cell membrane.**

**Figure 1 – figure supplement 2. Kir6.2\*-GFP is functionally similar to Kir6.2-GFP.**

71 (15–25%).

72 ANAP incorporation into Kir6.2 was achieved as described previously (*Chatterjee et al., 2013*; *Zagotta et al., 2016; Puljung et al., 2019*). Briefly, HEK-293T cells were co-transfected with a plasmid  
73 encoding a Kir6.2 construct with a C-terminal GFP tag and an amber stop codon (TAG) replacing  
74 the codon corresponding to amino acid position 311 (W311<sup>TAG</sup>-GFP) and a plasmid encoding an  
75 ANAP-specific tRNA/tRNA synthetase pair (pANAP). We also included a dominant negative eukary-  
76 otic ribosomal release factor (eRF-E55D) in our transfections, which has been shown to increase  
77 the amount of full-length, ANAP-labelled protein (*Schmied et al., 2014; Puljung et al., 2019*). When  
78 cultured in the presence of ANAP, full length, fully ANAP-labelled Kir6.2 protein was produced and  
79 successfully trafficked to the membrane in the presence of SUR1 (Figure 1—Figure supplement 1;  
80 see Materials and Methods). ANAP fluorescence from labelled channels can be separated from  
81 unincorporated ANAP or autofluorescence based on emission spectra (*Puljung et al., 2019*). How-  
82 ever, we found it much more convenient to first identify transfected cells or membrane fragments  
83 based on the presence of a GFP tag. Thus, we used GFP-tagged Kir6.2 constructs throughout this  
84 study, unless otherwise indicated.

85 In all our experiments, we measured currents in excised patches from cells expressing K<sub>ATP</sub>  
86 in the absence of Mg<sup>2+</sup>. Under such conditions, nucleotides can bind to both sites on SUR1, but  
87 no activation occurs, allowing inhibitory currents to be measured in isolation (*Gribble et al., 1998*;  
88 *Ueda et al., 1999; Puljung et al., 2019*). Kir6.2\*-GFP + SUR1 exhibited nearly identical sensitivity to  
89 ATP inhibition as Kir6.2-GFP + SUR1 (Figure 1—Figure supplement 2A), indicating that replacement  
90 of W311 with ANAP did not affect inhibition by K<sub>ATP</sub>. Both subunits also showed similar sensitiv-  
91 ity to TNP-ATP, which inhibited with a higher apparent affinity relative to ATP (Figure 1—Figure  
92

93 supplement 2B,C).

94 Kir6.2-GFP has been demonstrated to traffic to the plasma membrane in the absence of SUR1  
 95 (*John et al., 1998; Makhina and Nichols, 1998*). In a luminescence-based, surface-expression assay,  
 96 we did not detect HA-tagged Kir6.2\*-GFP at the plasma membrane in the absence of SUR1 (Fig-  
 97 ure 1—Figure supplement 1E). To verify that the currents measured in our experiments in which  
 98 Kir6.2\*-GFP was co-transfected with SUR1 were the result of Kir6.2\*-GFP + SUR1 and not Kir6.2\*-  
 99 GFP alone, we measured the sensitivity of currents to inhibition by the sulphonylurea tolbutamide,  
 100 a property conferred by the SUR1 subunit. Whereas currents from unlabelled wild-type Kir6.2-  
 101 GFP expressed in the absence of SUR1 were not affected by 100  $\mu$ M tolbutamide, both wild-type  
 102 Kir6.2-GFP and Kir6.2\*-GFP currents were inhibited to a similar extent by when expressed with  
 103 SUR1 (46.5%  $\pm$ 0.04% and 57.7%  $\pm$ 0.02%, respectively; Figure 1—Figure supplement 2D). The ex-  
 104 tent of block was similar to previous measurements of tolbutamide inhibition (*Tucker et al., 1997*),  
 105 confirming that Kir6.2\*-GFP was co-assembled with SUR1 at the plasma membrane.

106 To measure nucleotide binding, cells transfected with Kir6.2\*-GFP + SUR1 were briefly soni-  
 107 cated, leaving behind unroofed plasma membrane fragments (*Heuser, 2000; Zagotta et al., 2016;*  
 108 *Puljung et al., 2019*) containing ANAP-labelled  $K_{ATP}$  channels with the intracellular nucleotide-binding  
 109 sites exposed to the bath solution. The sample was excited with a 385 nm LED and emitted fluores-  
 110 cence from the membrane fragments was passed through a spectrometer, allowing us to separate  
 111 ANAP, GFP, and TNP-ATP fluorescence by peak wavelength (Figure 1E,F). As expected from FRET,  
 112 increasing the concentration of TNP-ATP caused a decrement in the ANAP peak at 472 nm and a  
 113 concomitant increase in the TNP-ATP peak at 561 nm (Figure 1F). We used the quenching of the  
 114 ANAP peak as a direct measure of TNP-ATP binding as this signal was specific to  $K_{ATP}$ . In contrast,  
 115 the peak TNP-ATP fluorescence may include contributions from both specific and non-specific nu-  
 116 cleotide binding. Due to the sharp cut-off of the GFP emission spectrum at shorter wavelengths,  
 117 our measurements of peak ANAP fluorescence were unaffected by the presence of the GFP tag on  
 118 Kir6.2.

119 We fit concentration-response data for TNP-ATP quenching with the Hill equation, to produce  
 120 estimates of apparent affinity and  $E_{max}$  (ANAP quenching at saturating concentrations of TNP-ATP;  
 121 Figure 1G).  $E_{max}$  was 93%, in good agreement with the 91% predicted by the Förster equation and  
 122 theoretical distance measurements (Figure 1D), suggesting that we were able to measure bind-  
 123 ing directly to the inhibitory site at Kir6.2. To confirm this, we introduced a well-studied neonatal  
 124 diabetes mutation (G334D) into the Kir6.2 binding site, which drastically reduces the sensitiv-  
 125 ity of the channel to inhibition by nucleotides (*Drain et al., 1998; Masia et al., 2007; Proks et al.,*  
 126 *2010*). Based on the cryo-electron microscopy structures of  $K_{ATP}$ , this mutation is expected to inter-  
 127 fere with nucleotide binding directly (Figure 1H inset, *Martin et al. (2017)*). The resulting construct  
 128 Kir6.2\*,G334D-GFP + SUR1 displayed drastically reduced ANAP quenching over the range of TNP-  
 129 ATP concentrations tested, with an  $E_{max}$  of 8%; again in good agreement with the predicted FRET ef-  
 130 ficiencies between ANAP at position 311 and TNP-ATP bound only to SUR1. We therefore conclude  
 131 that our binding measurements were specific for the inhibitory nucleotide-binding site on Kir6.2.  
 132 This observation is consistent with the interpretation that the G334D mutation causes neonatal  
 133 diabetes by preventing nucleotide binding. However, the observed loss in nucleotide-dependent

134 quenching in Kir6.2\*-G334D-GFP may also be due to an allosteric effect of the G334D mutation on  
 135 channel gating. We feel that this interpretation is unlikely, as G334D has been shown to have no  
 136 effect on the unliganded  $P_{open}$  of K<sub>ATP</sub> (*Proks et al., 2010*).

137 **Measuring current inhibition and nucleotide binding simultaneously.** The apparent affinity  
 138 of Kir6.2\*-GFP + SUR1 for TNP-ATP in unroofed membranes was 25.6 μM (Figure 1G and Table  
 139 1). This value is higher than the apparent affinity for nucleotide inhibition (6.2 μM) measured using  
 140 patch-clamp (Figure 1—Figure supplement 2C). However, both binding and current measurement  
 141 are a function of the intrinsic binding affinity, the channel  $P_{open}$ , and the ability of agonist, once  
 142 bound, to close the channel. Furthermore, the functional state of K<sub>ATP</sub> in unroofed membranes is  
 143 unclear. This is a particular problem with K<sub>ATP</sub> channels, which run down due to slow dissociation  
 144 of phosphatidylinositol 4,5-bisphosphate (PIP<sub>2</sub>), reducing the  $P_{open}$  over time even in the absence  
 145 of nucleotides (*Proks et al., 2016*).

146 As measuring either nucleotide binding or ionic currents in isolation only offers limited mecha-  
 147 nistic insight into inhibition of K<sub>ATP</sub>, we turned to patch-clamp fluorometry (PCF, *Proks et al. (2016)*;  
 148 *Zheng and Zagotta (2003)*). Using PCF, we can measure TNP-ATP binding to Kir6.2 and channel  
 149 activity simultaneously (Figure 2), providing us with direct access to the relationship between nu-  
 150 cleotide binding and channel function. We simultaneously measured fluorescence emission spec-  
 151 tra and ionic currents for Kir6.2\*-GFP + SUR1 in inside-out, excised membrane patches. As before,  
 152 all measurements were performed in the presence of Mg<sup>2+</sup> chelators, such that nucleotide inhi-  
 153 bition could be measured in the absence of activation (*Tucker et al., 1997; Gribble et al., 1998*).  
 154 Strikingly, current inhibition occurred at a lower range of concentrations compared to nucleotide  
 155 binding (Figure 2C,D). The apparent EC<sub>50</sub> for inhibition calculated from Hill fits was an order of  
 156 magnitude lower than the EC<sub>50</sub> for binding measured in the same patches (Figure 2C, Table 2).  
 157 We considered several different gating models to explain this observation. In each model, we as-  
 158 sumed the channel pore was able to open and close in the absence of ligand with an equilibrium  
 159 constant  $L$ , where  $P_{open} = L/(L + 1)$  and  $L > 0$ . This reflects the ability of K<sub>ATP</sub> to open and close  
 160 in the absence of nucleotides. Each model also had parameters representing the intrinsic binding  
 161 affinity to the closed state ( $K_A$ , where  $K_A > 0$ ) and the factor by which nucleotide binding favours  
 162 channel closure ( $D$ , where  $D < 1$ ).

163 Our simultaneous binding and current measurements were well fit with a Monod-Wyman-Changeux  
 164 (MWC)-type model (Figure 2D,E; *Monod et al. (1965)*) which has been previously proposed to explain  
 165 K<sub>ATP</sub> channel inhibition (*Enkvetachakul and Nichols, 2003; Craig et al., 2008; Vedovato et al., 2015*).  
 166 In our MWC-type model, each ligand binding event ( $K_A$ ) is independent and each bound ligand  
 167 favours the closed state by the same factor ( $D$ ). Simultaneous measurement of binding (fluores-  
 168 cence) and gating (current) allowed us to obtain well constrained fits to our model. To obtain free  
 169 parameter ( $L$ ,  $K_A$ ,  $D$ ) estimates and verify that each parameter was well and uniquely determined,  
 170 we employed a Bayesian Markov chain Monte Carlo (MCMC) method previously employed by Hines  
 171 et al. (*Hines et al., 2014*). Using this approach, we constructed posterior probability distributions  
 172 for the free parameters of our MWC-type model (Figure 2F, Table 3). Based on these distributions,  
 173 we estimated  $K_A = 2.1 \times 10^4 \text{ M}^{-1}$  ( $K_D = 47.9 \mu\text{M}$ ),  $L = 0.09$  ( $P_{open} = 0.08$ ), and  $D = 0.04$ . The very low  
 174  $D$  value indicates that nucleotide binding was tightly coupled to channel closure; i.e. nucleotides

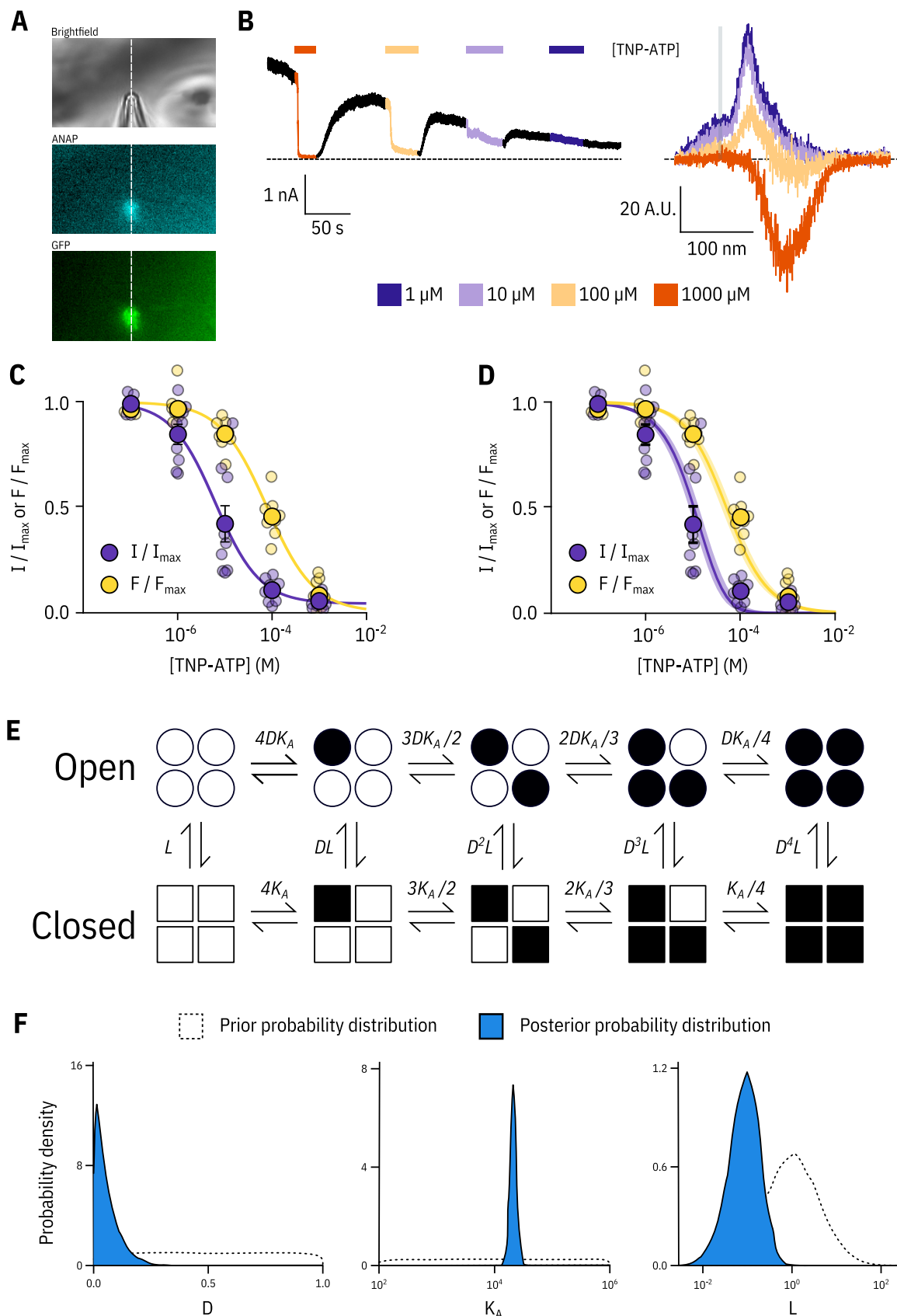


**Figure 2. Simultaneous measurements of nucleotide binding and channel current.**

**Figure 2. Simultaneous measurements of nucleotide binding and channel current.** **A.** Brightfield and fluorescence images of a patch pipette and excised, inside out patch expressing Kir6.2\*-GFP + SUR1, with the location of the centre of the spectrometer slit overlaid as a white, vertical line. **B.** Current (left) and spectra (right) acquired from the same excised, inside-out patch exposed to TNP-ATP and coloured according to concentration. **C.** Concentration-response ( $n = 9$ ) for TNP-ATP inhibition of Kir6.2\*-GFP + SUR1 currents ( $I/I_{max}$ ) and for quenching of ANAP fluorescence ( $F/F_{max}$ ). Both current inhibition and fluorescence quenching were fit to the Hill equation. Current inhibition:  $IC_{50} = 6.23 \mu\text{M}$ ,  $h = 0.92$ ,  $I_{max} = 0.96$ , fluorescence quenching:  $EC_{50} = 77.7 \mu\text{M}$ ,  $h = 0.87$ ,  $E_{max} = 1.00$ . **D.** The same data as in **C** fit to an MWC-type model. Solid curves represent the median fit; shaded areas represent the 95% quantile interval. Values for the fits are reported in the text and in Table 3. **E.** MWC-type model for inhibition of  $K_{ATP}$  by nucleotides. Open subunits are shown as circles; closed are shown as squares. Nucleotide-bound subunits are represented by filled symbols.  $L$ ,  $D$ , and  $K_A$  are defined in the text. **F.** Posterior probability distributions for the MWC-type model generated by MCMC fits to the data in **C** overlaid on the prior probability distribution (dashed line) for each parameter.

**Figure 2 – figure supplement 1. Fixing  $L$  does not affect estimates of  $D$  and  $K_A$ .**

**Figure 2 – figure supplement 2. Model selection.**

175 have a very strong preference for the closed state of the channel. The low value for  $D$  also explains  
 176 why the channels were nearly completely inhibited at TNP-ATP concentrations at which not all the  
 177 binding sites were occupied, as well as the degree to which channel inhibition is complete at sat-  
 178 urating concentrations of TNP-ATP. Our estimate of  $L$  was quite low and broadly distributed. We  
 179 repeated our fits with  $L$  fixed to a value consistent with previous single channel measurements (0.8,  
 180  $P_{open} = 0.45$ , *John et al. (1998)*; *Enkvetachakul et al. (2000)*; *Ribalet et al. (2006)*). This had only a very  
 181 small effect on our estimates of  $D$  and  $K_A$  (Figure 2—Figure supplement 1). The broad distribution  
 182 of  $L$  in our fit may represent current rundown which occurs during our patch-clamp recordings and  
 183 is expected to affect the open-closed equilibrium. Cross-correlation plots (in parameter space) of  
 184 the values derived from our fits produced well bounded ellipsoids, indicating that our parameters  
 185 were uniquely determined (Figure 2—Figure supplement 1A).

186 In addition to the full MWC-type model we considered alternate models (Figure 2—Figure sup-  
 187 plement 2). These included a model in which only the first binding event influences the open-closed  
 188 equilibrium of the channel (single-binding model; Figure 2—Figure supplement 2B, Table 3), and  
 189 an MWC-style model with an additional parameter  $C$  to allow for direct negative cooperativity be-  
 190 tween binding sites (negative cooperativity model; Figure 2—Figure supplement 2C, Table 3). The  
 191 single-binding model yielded very similar parameter estimates to our full MWC-type model (Figure  
 192 2—Figure supplement 2D, Table 3). This is a consequence of  $D$  being so low that even in the MWC-  
 193 type model most channels are closed when only a single nucleotide is bound. The cooperative  
 194 model improved our fits, but not enough to justify the inclusion of an additional free parameter  
 195 (see Discussion).

196 **Kir6.2-C166S affects the ability of bound nucleotides to close  $K_{ATP}$ .** To provide a rigorous  
 197 test as to whether our experimental system was capable of separating nucleotide binding from  
 198 subsequent channel gating, we introduced a mutation (Kir6.2-C166S) which increases  $P_{open}$  of  $K_{ATP}$   
 199 and decreases sensitivity of the channel to block by nucleotides (*Trapp et al., 1998*). C166 is located  
 200 near the bundle-crossing gate of Kir6.2 (Figure 3A). Other mutations at this site cause neonatal  
 201 diabetes (*Flanagan et al., 2006*; *Gloyn et al., 2006*).

202 In unroofed membranes, Kir6.2\*-C166S-GFP + SUR1 bound TNP-ATP with an  $EC_{50}$  very similar  
 203 to that of Kir6.2\*-GFP + SUR1 (Figure 3B, 32.0  $\mu\text{M}$  and 25.6  $\mu\text{M}$ , respectively), which suggests only a

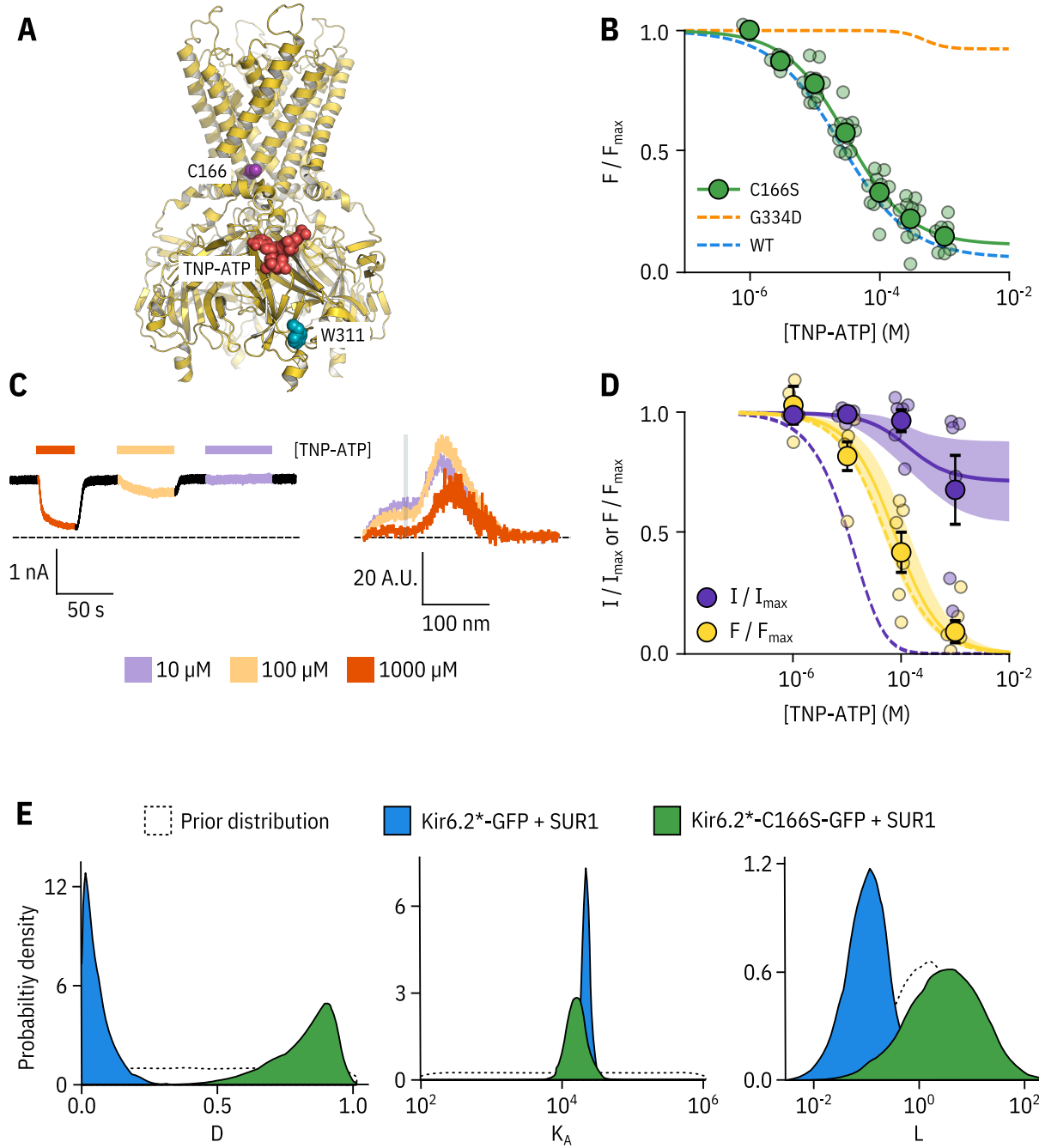


**Figure 3. Kir6.2-C166S disrupts current inhibition, not nucleotide binding.** **A.** Cartoon (from PDB accession #6BAA) showing the location of Kir6.2-C166 (purple) relative to the inhibitory nucleotide binding site (TNP-ATP from PDB accession #5XW6 shown in red). W311 is shown as blue spheres. **B.** Concentration dependence of TNP-ATP binding to unroofed membrane fragments expressing Kir6.2\*-C166S-GFP + SUR1 shown in green, expressed as quenching of ANAP fluorescence. The Hill fits shown previously for Kir6.2\*-GFP + SUR1 and Kir6.2\*-G334D-GFP are shown in blue and orange dashed curves, respectively. Kir6.2\*-C166S-GFP + SUR1:  $EC_{50} = 32.0 \mu\text{M}$ ,  $h = 0.92$ ,  $E_{max} = 0.96$ ,  $n = 12$ . **C.** Representative current and fluorescence traces recorded simultaneously from an excised patch expressing Kir6.2\*-C166S-GFP + SUR1. Exposure to different concentrations of TNP-ATP are shown by colour. **D.** Concentration-response ( $n = 6$ ) for TNP-ATP inhibition of Kir6.2\*-C166S-GFP + SUR1 currents ( $I/I_{max}$ ) and for quenching of ANAP fluorescence ( $F/F_{max}$ ). Data were fit with the MWC-type model. Solid curves represent the median fits and shaded areas indicate the 95% quantile intervals. Dashed curves represent the previous median fits of the MWC-type model to the Kir6.2\*-GFP + SUR1 data from Figure 2D. Parameter estimates are reported in Table 3. **E.** Posterior probability distributions for the full MWC-type model fit to Kir6.2\*-C166S-GFP + SUR1 or Kir6.2\*-GFP + SUR1 (data from Figure 2F) overlaid on the prior probability distribution.

**Figure 3 – figure supplement 1. Fixing the  $L$  parameter does not affect the other two parameters.**

204 small change in nucleotide affinity. This is an unexpected finding, as one might expect that an in-  
 205 crease in  $P_{open}$  would allosterically cause a decrease in the apparent affinity for inhibitory nucleotide  
 206 binding. To resolve this conflict, we again turned to PCF (Figure 3C,D). Rundown was much slower  
 207 for Kir6.2\*-C166S-GFP + SUR1, which may reflect the increased  $P_{open}$  of this construct. Measuring  
 208 current inhibition in combination with nucleotide binding confirmed that whereas the apparent  
 209 nucleotide affinity was unchanged by the C166S mutation, current inhibition occurred at much  
 210 higher concentrations compared to binding (Figure 3D). How can we explain this paradox? Fits of  
 211 the data with our MWC-type model (Figure 3D,E) suggest that, in addition to the expected effect  
 212 on  $L$ , the C166S mutation profoundly affects the ability of bound ligand to close the channel ( $D$ )  
 213 without affecting  $K_A$  (Figure 3E, Table 3). We propose that, in addition to increasing the  $P_{open}$  of the  
 214 channel, C166 is also important in the transduction pathway from the inhibitory nucleotide binding  
 215 site on Kir6.2 to the channel gate.

216 **Exploring the effect of SUR1 on nucleotide inhibition of  $K_{ATP}$ .** SUR1 plays a complex role  
 217 in the regulation of Kir6.2. It increases the  $P_{open}$  of the channel and allows for the activation of  
 218 the channel by Mg-nucleotides (Nichols et al., 1996; Tucker et al., 1997; Babenko and Bryan, 2003;  
 219 Chan et al., 2003; Fang et al., 2006). However, it also increases the sensitivity of Kir6.2 to nucleotide  
 220 inhibition (Babenko and Bryan, 2003; Chan et al., 2003; Fang et al., 2006). To understand the ef-  
 221 fect of SUR1 on nucleotide inhibition of  $K_{ATP}$ , we expressed Kir6.2\*-GFP in the absence of SUR1 in  
 222 unroofed membranes and measured TNP-ATP binding (Figure 4A). We found only a small increase  
 223 (approximately 1.5-fold) in apparent  $EC_{50}$  compared to the same construct in the presence of SUR1  
 224 (37.6  $\mu$ M and 25.6  $\mu$ M respectively). Unfortunately, we were unable to achieve high enough expres-  
 225 sion of Kir6.2\*-GFP alone to carry out PCF experiments in the absence of SUR1. However, we were  
 226 able to measure currents from unlabelled Kir6.2-GFP alone (Figure 4B). As expected Kir6.2-GFP  
 227 alone was much less sensitive to inhibition by TNP-ATP than Kir6.2-GFP + SUR1.

228 To determine whether SUR1 had complex effects on nucleotide binding that were not revealed  
 229 in equilibrium binding experiments, we measured the time-course of TNP-ATP binding and unbind-  
 230 ing to Kir6.2\*-GFP expressed in unroofed membranes in the absence and presence of SUR1 (Figure  
 231 4C). We fit the apparent on- ( $k_{obs}$ ) and off-rates ( $k_{off}$ ) for different concentrations of TNP-ATP to sin-  
 232 gle exponential decays (equation 1). As expected, the off-rate was independent of [TNPATP]. We  
 233 determined  $k_{on}$  from the slope of linear fits to  $k_{obs}$  as a function of nucleotide concentration, where  
 234  $k_{obs} = k_{on} * [TNPATP] + k_{off}$  (Figure 4D).  $k_{on}$  for TNP-ATP binding was nearly identical in the pres-  
 235 ence and absence of SUR1 (5641  $M^{-1} s^{-1}$  vs. 5564  $M^{-1} s^{-1}$ , respectively). However, the mean  $k_{off}$   
 236 was roughly twice as fast in the absence of SUR1 (0.36  $s^{-1}$  in the absence of SUR1 vs. 0.16  $s^{-1}$  in the  
 237 presence of SUR1). Measuring  $k_{on}$  and  $k_{off}$  also provided an independent measure of  $EC_{50}$ , if we as-  
 238 sume a single-step process with  $EC_{50}$  given by  $k_{off}/k_{on}$ . Using this method, we calculated the  $EC_{50}$   
 239 for Kir6.2\*-GFP + SUR1 to be 28.3  $\mu$ M, quite close to the 25.6  $\mu$ M derived from steady-state mea-  
 240 surements. The  $EC_{50}$  calculated from the TNP-ATP binding kinetics for Kir6.2\*-GFP in the absence  
 241 of SUR1 was 64.0  $\mu$ M, higher than the value of 37.6  $\mu$ M derived from steady-state measurements.  
 242 We believe this discrepancy arises from the variability in our rate measurements. Nevertheless,  
 243 the two-fold decrease in  $k_{off}$  for TNP-ATP in the presence of SUR1 suggests that SUR1 stabilises  
 244 nucleotide binding to Kir6.2. However, these binding measurements do not rule out an indirect,

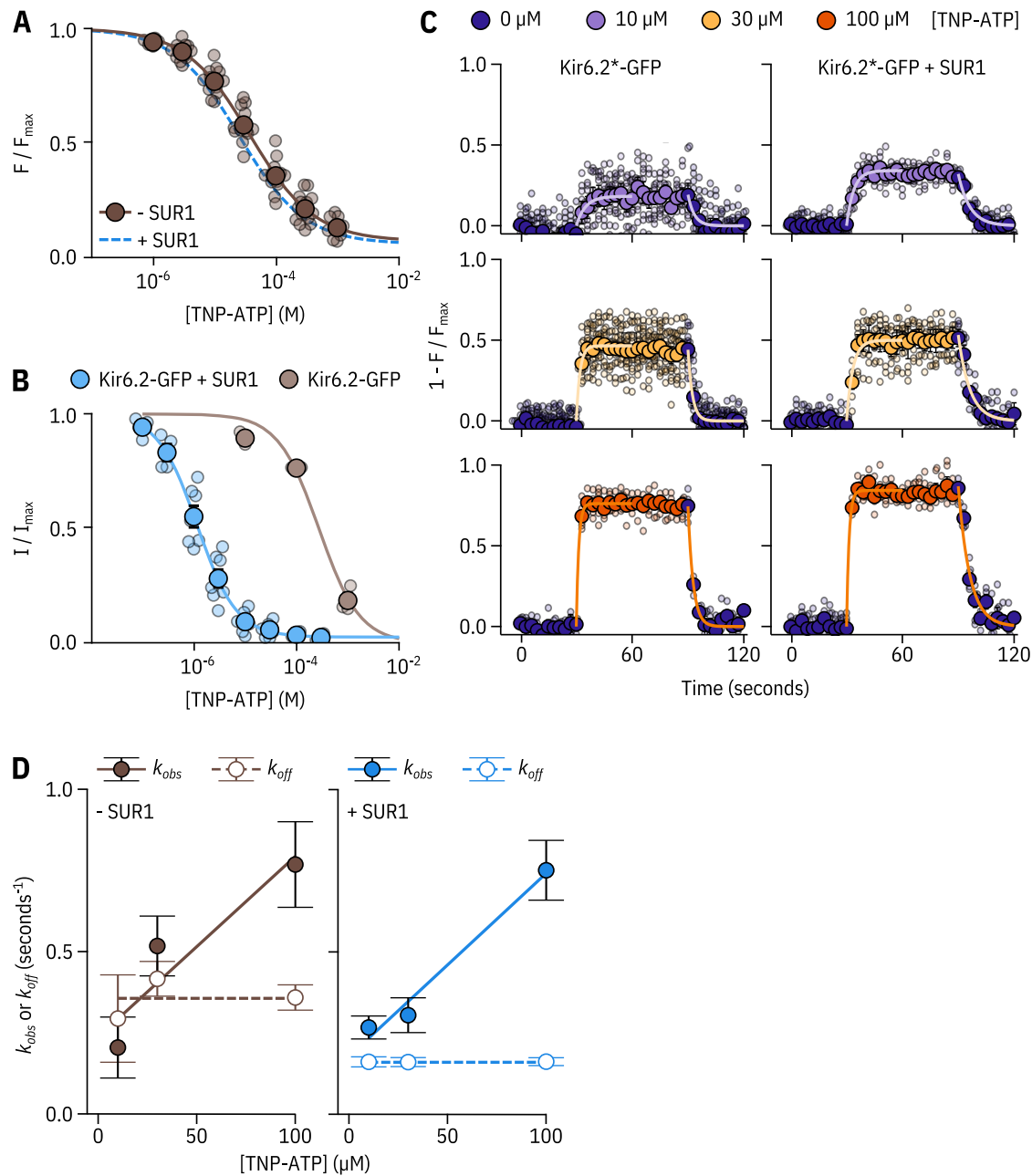


**Figure 4. SUR1 affects the apparent affinity for and kinetics of nucleotide binding to Kir6.2.** **A.** Concentration dependence of TNP-ATP binding to unroofed membrane fragments expressing Kir6.2\*-GFP without SUR1 (brown), expressed as quenching of ANAP fluorescence. The smooth curve is a descriptive Hill fit. Kir6.2\*-GFP (no SUR1):  $EC_{50} = 37.6 \mu\text{M}$ ,  $h = 0.83$ ,  $E_{max} = 0.92$ ,  $n = 14$ . The Hill fit to Kir6.2\*-GFP + SUR1 is shown as a blue dashed curve. **B.** Concentration-response curve for TNP-ATP inhibition of Kir6.2-GFP (no ANAP label) without or without co-expression of SUR1, measured in excised, inside-out patches. Kir6.2-GFP + SUR1:  $EC_{50} = 1.17 \mu\text{M}$ ,  $h = 1.14$ ,  $E_{max} = 0.97$ ,  $n = 7$ ; Kir6.2-GFP (no SUR1):  $EC_{50} = 273 \mu\text{M}$ ,  $h = 1.09$ ,  $E_{max} = 1.00$ ,  $n = 3$ . **C.** Time-courses of TNP-ATP binding and unbinding to Kir6.2\*-GFP expressed in unroofed membrane fragments in the presence or absence of SUR1. Data are displayed as  $1 - F/F_{max}$  so that upward deflections indicate binding and downward deflections indicate unbinding. Small data points represent individual experiments. Overlaid are larger points representing the mean  $\pm$  standard error at each time point. The smooth curves are single exponential fits to the wash-on or wash-off of a given concentration of TNP-ATP. **D.** Rate constants ( $k_{obs}$  and  $k_{off}$ ) from the exponential fits as in **C** are plotted as functions of the TNP-ATP concentration. Linear fits to  $k_{obs}$  were performed using equation 3. Kir6.2\*-GFP (no SUR1):  $k_{on} = 5560 \text{ M}^{-1} \text{ s}^{-1} \pm 2180 \text{ M}^{-1} \text{ s}^{-1}$ ,  $k_{off} = 0.24 \text{ s}^{-1} \pm 0.13 \text{ s}^{-1}$ ,  $n = 2-6$  per concentration. Kir6.2\*-GFP + SUR1:  $k_{on} = 5640 \text{ M}^{-1} \text{ s}^{-1} \pm 812 \text{ M}^{-1} \text{ s}^{-1}$ ,  $k_{off} = 0.18 \text{ s}^{-1} \pm 0.05 \text{ s}^{-1}$ ,  $n = 3-4$  per concentration. Dashed lines indicate the mean rates measured for wash-off experiments ( $k_{off}$ ) from all test concentrations combined. Kir6.2\*-GFP (no SUR1):  $k_{off} = 0.36 \text{ s}^{-1} \pm 0.04 \text{ s}^{-1}$ . Kir6.2\*-GFP + SUR1:  $k_{off} = 0.16 \text{ s}^{-1} \pm 0.0004 \text{ s}^{-1}$ .

245 allosteric effect of SUR1 on nucleotide binding. To explore the effect of SUR1 more rigorously, we  
 246 again turned to PCF.

247 As Kir6.2\*-GFP expression in the absence of SUR1 was not sufficient for PCF recordings, we  
 248 took a mutational approach to better understand the role of SUR1 in inhibitory nucleotide binding.  
 249 SUR1-K205 is located in the L0 linker of SUR1, which connects the first set of transmembrane do-  
 250 mains (TMD0) to the ABC core structure (Figure 1A, Figure 5A; *Martin et al. (2017); Puljung (2018)*).  
 251 This loop is adjacent to the inhibitory nucleotide-binding site on Kir6.2 and the interface between  
 252 neighbouring Kir6.2 subunits. Mutations at K205 were previously shown to reduce sensitivity of  
 253  $K_{ATP}$  to nucleotide-dependent inhibition (?). Other mutations in L0 are associated with neonatal  
 254 diabetes (*Ashcroft et al., 2017*) and PHHI (*Snider et al., 2013*).

255 We introduced a charge neutralization (alanine, K205A) and a charge reversal (glutamate, K205E)  
 256 mutation at this position and measured simultaneous nucleotide binding and current inhibition  
 257 with PCF (Figure 5B,C,D). The binding and inhibition curves for TNP-ATP almost perfectly overlaid  
 258 for the SUR1-K205A mutant (Figure 5C). The same was also true for SUR1-K205E (Figure 5D). Data  
 259 were fit with the MWC-type model as before. Mutating K205 to an alanine or a glutamate resulted  
 260 in an apparent decrease in nucleotide binding affinity (Figure 5C,D,E). This was reflected by a de-  
 261 crease in the estimated  $K_A$  for TNP-ATP, which correlated with the degree of conservation of the  
 262 mutation, i.e. we observed a larger effect for the charge reversal compared to the charge neutral-  
 263 ization mutation (Figure 5E). However, in addition to direct effects of K205 on nucleotide binding,  
 264 we also observed a shift in  $D$  for both mutations (Figure 5E). This suggests a dual role for SUR1 in  
 265  $K_{ATP}$  inhibition, both in contributing to nucleotide binding and in stabilizing the nucleotide-bound  
 266 closed state.

## 267 Discussion

268 We have developed a novel approach that allows for site-specific measurement of nucleotide bind-  
 269 ing to  $K_{ATP}$  and concomitant measurements of channel current. Performing these measurements  
 270 simultaneously allowed us to examine nucleotide regulation of  $K_{ATP}$  function in great detail. We  
 271 used a Bayesian approach to fit models to our combined fluorescence/current data sets to extract  
 272 meaningful functional parameters with a minimum of prior assumptions. Such insights would not  
 273 be possible from experiments in which macroscopic currents or binding were measured in isol-  
 274 ation.

275 PCF has been used successfully by other labs to simultaneously measure ligand binding and  
 276 gating in HCN channels (*Biskup et al., 2007; Kusch et al., 2010; Wu et al., 2011*). These groups mea-  
 277 sured fluorescence from a cyclic nucleotide analogue that increased its quantum yield when bound,  
 278 minimizing background fluorescence from unbound ligand. Additional background subtraction  
 279 could be performed by imaging the patches using confocal microscopy such that a region corre-  
 280 sponding to the patch membrane could be computationally selected, thus omitting background  
 281 fluorescence from the surrounding solution (*Biskup et al., 2007; Kusch et al., 2010*). In our PCF ex-  
 282 periments, we used a FRET-based approach to measure ligand binding. We acquired fluorescence  
 283 emission spectra, such that donor fluorescence could be separated from acceptor fluorescence by  
 284 wavelength. This allowed us to directly assess binding from the quenching of donor fluorescence,

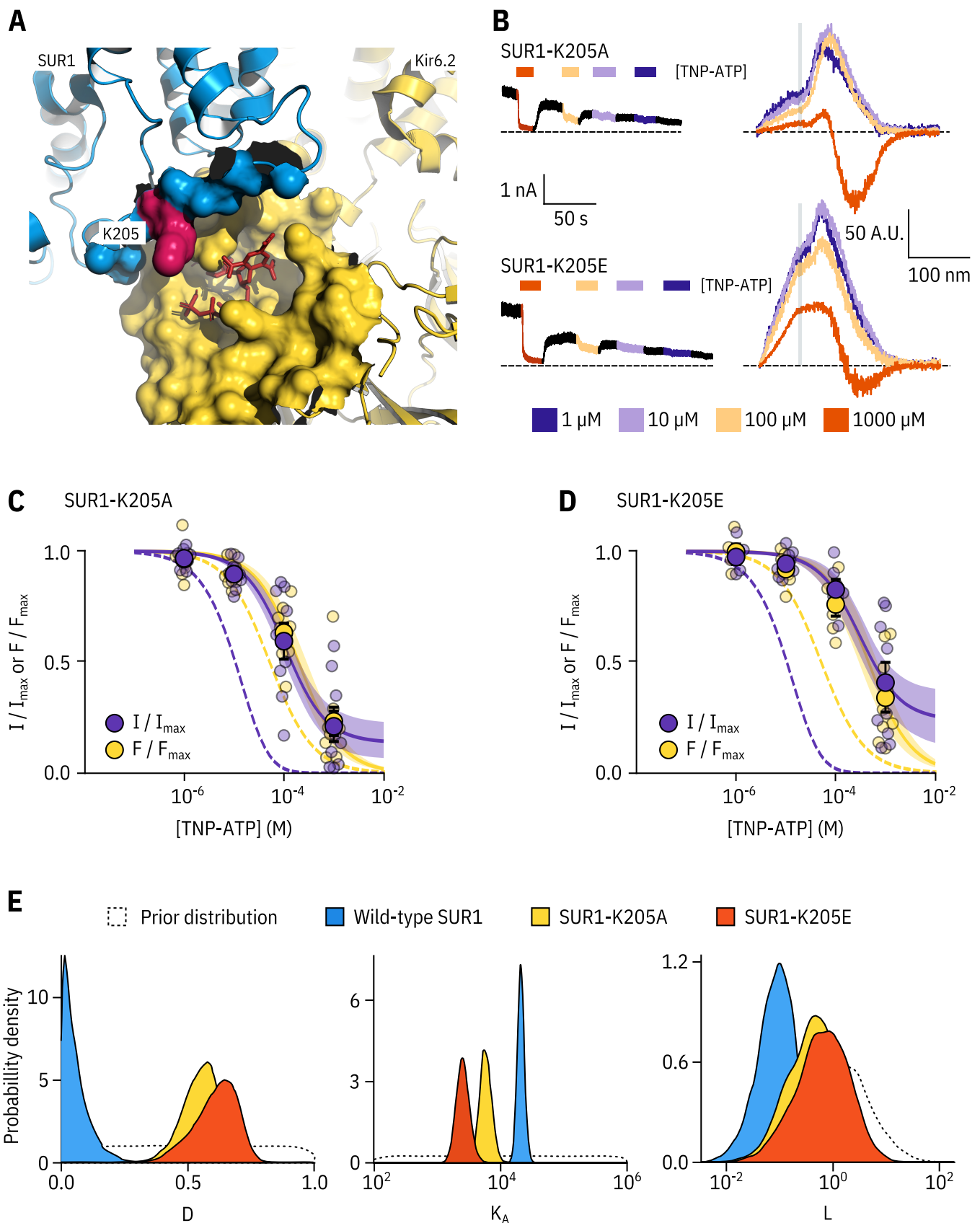


**Figure 5. SUR1-K205 modulates both nucleotide affinity and inhibition of Kir6.2.**

**Figure 5. SUR1-K205 modulates both nucleotide affinity and inhibition of Kir6.2.** **A.** Hydrophobic surface representation of Kir6.2 (yellow, PDB accession #6BAA) and SUR1 (blue, PDB accession #6PZI). Residue K205 on SUR1 is highlighted in pink. As this residue was built as an alanine in the structure, we used the mutagenesis tool in PyMol to insert the native lysine residue. A docked TNP-ATP molecule is shown in red. **B.** Representative current and fluorescence traces acquired simultaneously from excised patches expressing Kir6.2\*-GFP with SUR1-K205A or SUR1-K205E. **C,D.** Concentration-response for TNP-ATP inhibition of currents ( $I/I_{max}$ ) and for quenching of ANAP fluorescence ( $F/F_{max}$ ) in excised inside-out membrane patches expressing Kir6.2\*-GFP + SUR1-K205A (**C**,  $n = 9$ ) or Kir6.2\*-GFP + SUR1-K205E (**D**,  $n = 9$ ). Data were fit to the MWC-type model. Solid curves represent the median fits and shaded areas indicate the 95% quantile intervals. Fits to Kir6.2\*-GFP + wild-type SUR1 are shown as dashed curves. **E.** Posterior probability distributions for the full MWC-type model fit to Kir6.2\*-GFP co-expressed with wild-type SUR1 (fits from Figure 2), SUR1-K205A and SUR1-K205E overlaid on the prior probability distribution.

**Figure 5 – figure supplement 1. Fixing the  $L$  parameter does not drastically affect the fits to the SUR1-K205A or SUR1-K205E data.**

**Figure 5 – figure supplement 2. Comparing the ability of each model to explain the data.**

which was specific to  $K_{ATP}$ . FRET also provided the spatial sensitivity necessary to discriminate between nucleotide binding directly to Kir6.2 and to the nucleotide-binding sites of SUR1. We assume that any TNP-ATP bound non-specifically to our membranes would be too far from Kir6.2 to cause appreciable FRET. This assumption was confirmed by the lack of FRET between TNP-ATP and a Kir6.2\*-GFP mutant (G334D), in which nucleotide binding was severely disrupted (Figure 1H).

Previous studies have suggested that  $K_{ATP}$  inhibition follows an MWC-type model (Trapp et al., 1998; Enkvetachakul and Nichols, 2003; Drain et al., 2004; Craig et al., 2008; Vedovato et al., 2015). The majority of this earlier work was performed using single-channel measurements of mutated and/or concatenated channel subunits. In this study, we confirm these results using minimally perturbed channels with nucleotide sensitivity similar to that of wild-type  $K_{ATP}$  (Figure 1—Figure supplement 2A). By using an MCMC approach to model fitting, we can also evaluate our models to assess how well the derived parameters were determined by the data. MCMC fits provide a basis for determining credible intervals for our parameter estimates. This allows for direct comparison of values derived from wild-type and different mutant constructs.

Although we did not explicitly include the effects of  $PIP_2$  on  $K_{ATP}$  gating in our model formulations, we assumed that the effects of  $PIP_2$  on  $P_{open}$  were implicitly modelled in our parameter  $L$ ; i.e. rundown due to dissociation of  $PIP_2$  manifests as a decrease in  $L$  rather than a change in the number of channels. Although we were able to extract identifiable parameter estimates for  $L$ ,  $D$  and  $K_A$ , our estimates of  $L$  for each model we considered were appreciably less well constrained than for the other parameters. We expect that this uncertainty arises from measuring a heterogeneous population of channels with regard to  $PIP_2$  binding. Fixing  $L$  to values derived from the literature (Figure 2—Figure supplement 1, Figure 3—Figure supplement 1, Figure 5—Figure supplement 1, Figure 5—Figure supplement 2) allowed us to extract estimates for  $D$  and  $K_A$  that were functionally identical to those derived from unconstrained fits, suggesting that the uncertainty of  $L$  does not affect our inferences for these other parameters. Therefore, PCF represents a robust means to compare  $K_A$  and  $D$  between different mutated  $K_{ATP}$  constructs without worrying about the confounding effects of rundown.

Previous studies suggest that, whereas  $K_{ATP}$  closure occurs via a concerted mechanism, individual nucleotide binding events at Kir6.2 are not equivalent (Markworth et al., 2000). Earlier attempts

314 to determine the stoichiometry of inhibitory nucleotide binding to Kir6.2 (i.e. how many ATPs must  
 315 bind to induce channel closure) have produced models ranging from those in which binding of a  
 316 single nucleotide completely shuts  $K_{ATP}$  to an MWC-type model in which each binding event is in-  
 317 dependent and contributes equally to channel closure (*Trapp et al., 1998; Markworth et al., 2000;*  
*318 Enkvetachakul and Nichols, 2003; Drain et al., 2004; Wang et al., 2007; Craig et al., 2008; Vedovato*  
*319 et al., 2015*). To resolve this controversy, we fit our data with both single-binding and MWC-type  
 320 models. At very low values for  $D$ , such as we derived from our experiments, the predictions of both  
 321 models are functionally very similar. Even in our MWC-type model, we expect most  $K_{ATP}$  channels  
 322 to be closed when just one molecule of nucleotide is bound.

323 It has been proposed that there is direct negative cooperativity between binding events at dif-  
 324 ferent subunits on Kir6.2 (*Wang et al., 2007*). We fit our data to an extended MWC-type model  
 325 including an additional free parameter ( $C$ ), representing negative binding cooperativity between  
 326 subunits (Figure 2—Figure supplement 2). Not surprisingly this model improved the fit to our data  
 327 as assessed by the Bayes factor, which represents the marginal likelihood of one model over an-  
 328 other to explain our observations (*Wagenmakers, 2007; Gronau et al., 2017*). We also tested the  
 329 cooperative model using approximate leave-one-out cross validation, which assesses the ability of  
 330 a model to predict new or out-of-sample data using in-sample fits. Although in this work, we are pri-  
 331 marily concerned with the inferences made from our fits, the ability of a model to make predictions  
 332 is a good measure of its usefulness. Based on this criterion, the cooperative model has no more  
 333 predictive accuracy than either the MWC-type model or the single-binding model. Therefore, the  
 334 inclusion of an additional free parameter is not justified. Furthermore, whereas the cooperative  
 335 model yielded good fits with identifiable parameters for Kir6.2\*-GFP + SUR1 channels, it failed to  
 336 do so for all the mutants considered. Thus, this model did not allow for direct comparison between  
 337 constructs. However, it remains a possibility that these mutations function in part by abolishing  
 338 binding cooperativity between subunits.

339 We performed all our experiments on mutated, tagged channels using a fluorescent derivative  
 340 of ATP. This allowed us to fit mechanistic models and readily compare between mutated constructs  
 341 that affect nucleotide inhibition of  $K_{ATP}$ . This raises an obvious question: how relevant are our  
 342 findings to inhibition of wild-type  $K_{ATP}$  by ATP? In a previous paper, we estimated  $D$  and  $K_A$  from  
 343 an MWC-type model based on fits to published data for ATP inhibition of wild-type Kir6.2 + SUR1  
*(Proks et al., 2010; Vedovato et al., 2015)*. The value we obtained for  $D$  (0.03) was quite similar to  
 345 that we report here from our PCF measurements (0.04). We also obtained a similar estimate for  
 346  $K_A$  in our previous model ( $3.0 \times 10^4 \text{ M}^{-1}$  vs  $2.1 \times 10^4 \text{ M}^{-1}$  from our PCF experiments). Despite ob-  
 347 taining similar parameters, past experiments in which only ionic currents were measured, did not  
 348 allow us to distinguish between competing gating models. Measuring currents and fluorescence  
 349 simultaneously allowed for better model selection and aided in our ability to identify constrained  
 350 parameters.

351 We compared the parameters derived for inhibitory nucleotide binding to those estimated for  
 352 nucleotide activation of  $K_{ATP}$  based on experiments in which currents and binding were measured  
 353 in separate preparations (*Puljung et al., 2019*). In those experiments, we estimated a value for  $E$ ,  
 354 the factor by which binding of MgTNP-ADP to SUR1 stabilized channel opening, of 2.2. Although this

355 value was derived using a different nucleotide, it still provides an approximate basis for comparing  
 356 the coupling of nucleotide stimulation through SUR1 to nucleotide inhibition via binding to Kir6.2.  
 357 If both activation and inhibition proceed via MWC-type models, the open closed equilibrium at sat-  
 358 urating nucleotide concentrations is given by  $L$  multiplied by  $E^4$  or  $D^4$ , respectively. The degree of  
 359 stabilization of the open state of  $K_{ATP}$  can be calculated as  $-RT \ln E^4$  for activation. Stabilization  
 360 of the closed state is given by  $-RT \ln D^4$ . Based on our observations, saturating concentrations of  
 361 MgTNP-ADP stabilized the open state by  $-1.9 \text{ kcal mol}^{-1}$  ( $-7.9 \text{ kJ mol}^{-1}$ ). At saturating concentra-  
 362 tions, TNP-ATP stabilized the closed state of  $K_{ATP}$  by  $-7.6 \text{ kcal mol}^{-1}$  ( $31.8 \text{ kJ mol}^{-1}$ ). Thus, at condi-  
 363 tions under which both excitatory and inhibitory nucleotide binding sites are saturated, inhibition  
 364 dominates, which is consistent with published measurements of wild-type  $K_{ATP}$  in the presence of  
 365  $Mg^{2+}$  (). In our previous study, we estimated  $K_A$  for MgTNP-ADP binding to the stimulatory second  
 366 nucleotide binding site of SUR1 to be  $5.8 \times 10^4 \text{ M}^{-1}$  ( $K_D = 17 \mu\text{M}$ ), higher affinity than the  $K_A$  we  
 367 report here for TNP-ATP binding to the inhibitory site on Kir6.2 ( $2.1 \times 10^4 \text{ M}^{-1}$ ,  $K_D = 48 \mu\text{M}$ ). Higher  
 368 affinity binding to the stimulatory site may explain the ability of MgADP to increase  $K_{ATP}$  currents  
 369 in the presence of ATP (Gribble et al., 1998). This phenomenon may also explain the bell-shaped  
 370 MgADP concentration-response curve for  $K_{ATP}$ , which shows an increase in current at low concen-  
 371 trations, followed by inhibition at higher concentrations (Proks et al., 2010; Vedovato et al., 2015).  
 372 Future experiments in which activation and inhibition are measured by PCF for the same ligand  
 373 will allow us to model the complex response of  $K_{ATP}$  under conditions where all three nucleotide  
 374 binding sites simultaneously affect channel gating (i.e. in the presence of  $Mg^{2+}$ ).

375 Mutations that cause neonatal diabetes reduce the sensitivity of  $K_{ATP}$  to nucleotide inhibition,  
 376 and reduction in nucleotide sensitivity is broadly correlated with disease severity (McTaggart et al.,  
 377 2010). We studied two residues on Kir6.2 that have been implicated in diabetes and have been  
 378 proposed to affect nucleotide sensitivity via different mechanisms. We find that G334D drastically  
 379 reduced the apparent affinity for nucleotide binding to  $K_{ATP}$  in unroofed membranes. In our MWC-  
 380 type models, this could only be explained by a dramatic decrease in  $K_A$ . This corroborates earlier  
 381 hypotheses that mutating G334 directly disrupts inhibitory nucleotide binding to Kir6.2 (Drain et al.,  
 382 1998). Due to poor expression, we were unable to test this construct using PCF. Therefore, we could  
 383 not obtain accurate estimates of  $K_A$  and  $D$ .

384 In contrast to G334D, the C166S mutation does not directly affect nucleotide binding to Kir6.2,  
 385 but rather disrupts the ability of bound nucleotide to close the channel. This contributes to the  
 386 decreased nucleotide sensitivity which was previously attributed solely to an increased  $P_{open}$ . In  
 387 the future, we hope to use this rigorous approach to assess a whole panel of neonatal diabetes  
 388 mutations in Kir6.2 to better understand the mechanism by which they cause disease.

389 Using PCF allowed us to probe more deeply into the role of SUR1 in regulating nucleotide inhibi-  
 390 tion of  $K_{ATP}$ . The cytoplasmic L0 loop of SUR1 was previously implicated in modulation of  $P_{open}$  and  
 391 nucleotide sensitivity of Kir6.2 (Babenko and Bryan, 2003; Chan et al., 2003; Pratt et al., 2012). We  
 392 find that, in addition to directly contributing to tighter nucleotide binding at Kir6.2, SUR1 plays a  
 393 critical role in preferentially stabilising the closed state of the channel when nucleotides are bound.  
 394 Whereas a single nucleotide-binding event is sufficient for channel closure when Kir6.2 is associ-  
 395 ated with wild-type SUR1, mutating residue K205 reduced the ability of a single nucleotide to close

396 the channel. This difference manifests in both our MWC-type and single-binding models.

397 In addition to providing mechanistic insights into disease-associated mutations in Kir6.2, our  
 398 PCF-based approach allows us to probe the interactions between Kir6.2 and SUR1 on two different  
 399 levels. As we show here, we can use this method to examine the effects of SUR1 on inhibitory  
 400 nucleotide binding to Kir6.2. We can also adapt this method to study activation of Kir6.2 by nu-  
 401 cleotides bound to the stimulatory sites on SUR1. Mutations in SUR1 that cause neonatal dia-  
 402 betes may do so by disrupting inhibitory binding/gating or enhancing the stimulatory effects of  
 403 nucleotides. The formalism developed in this study provides a rigorous way to mechanistically  
 404 assess the effects of these mutations. Our approach should be readily adaptable to the study of  
 405 other nucleotide-gated channels including the cystic fibrosis transmembrane conductance regula-  
 406 tor (CFTR, also an ABC-family protein) and purinergic P2X receptors.

## 407 Materials and Methods

### 408 Key resources table.

Reagent type (species) or resource	Designation	Source or reference	Identifiers
Cell line	HEK-293T	LGC Standards (ATCC CRL-3216)	
Transfected construct ( <i>Escherichia. coli</i> )	pANAP	Addgene	
Transfected construct ( <i>Aequorea victoria</i> )	pcDNA4/TO pCGFP_EU	Gouaux Laboratory (Vollum Institute, Portland OR USA)	
Transfected construct ( <i>Homo sapiens</i> )	peRF1-E55D	Chin Laboratory (MRC Laboratory of Molecular Biology, Cambridge UK)	
409 Antibody	Anti-HA High Affinity; Rat monoclonal antibody (clone 3F10)	Roche	(Roche Cat# 11867423001, RRID:AB_10094468)
Antibody	Peroxidase-AffiniPure Goat Anti-Rat IgG (H + L) antibody	Jackson ImmunoResearch Labs	(Jackson ImmunoResearch Labs Cat# 112-035-003, RRID:AB_2338128)
Chemical compound, drug	trinitrophenyl-ATP (TNP-ATP)	Jena Bioscience (Jena, Germany)	
Chemical compound, drug	L-3-(6-acetyl naphthalen-2-ylamino)-2-aminopropionic acid	Asis Chemicals (Waltham, MA)	

### 410 Molecular biology.

411 Human Kir6.2 and SUR1 were subcloned into pcDNA4/TO and pCGFP\_EU vectors for expression  
 412 of wild-type and GFP-tagged constructs, respectively. pcDNA4/TO and pANAP were obtained from  
 413 Addgene. peRF1-E55D and pCGFP\_EU were kind gifts from the Chin Laboratory (MRC Laboratory  
 414 of Molecular Biology, Cambridge, UK) and the Gouaux Laboratory (Vollum Institute, Oregon, USA)

415 respectively. Amber stop codons and point mutations were introduced using the QuikChange XL  
 416 system (Stratagene; San Diego, CA). All constructs were confirmed by DNA sequencing (DNA Se-  
 417 quencing and Services, University of Dundee, Scotland).

#### 418 **Cell culture and channel expression.**

419 HEK-293T cells were obtained from and verified/tested for mycoplasma by LGC standards (ATTC  
 420 CRL-3216, Middlesex, UK). Our working stock tested negative for mycoplasma contamination us-  
 421 ing the MycoAlert Mycoplasma Detection Kit (Lonza Bioscience; Burton on Trent, UK). Cells were  
 422 plated onto either poly-l-lysine coated borosilicate glass coverslips (VWR International; Radnor, PA)  
 423 or poly-d-lysine coated glass-bottomed FluoroDishes (FD35-PDL-100, World Precision Instruments).  
 424 ANAP-tagged Kir6.2 constructs were labelled using amber stop codon suppression as described by  
 425 Chatterjee et al (*Chatterjee et al., 2013*). Transfections were carried out 24 hours after plating  
 426 using TransIT-LT1 (Mirus Bio LLC; Madison, WI) at a ratio of 3  $\mu$ l per  $\mu$ g of DNA. Unless specified  
 427 otherwise, all transfections included a Kir6.2 construct with an amber stop codon (TAG) at posi-  
 428 tion 311 (Kir6.2-W311<sup>TAG</sup>), SUR1, pANAP and eRF1-E55D in the ratio 0.5:1.5:1:1. Transfected cells  
 429 cultured in Dulbecco's Modified Eagle Medium (Sigma; St. Louis, MO) + 10% foetal bovine serum,  
 430 100 U ml<sup>-1</sup> penicillin and 100  $\mu$ g ml<sup>-1</sup> streptomycin (Thermo Fisher Scientific; Waltham, MA) sup-  
 431 plemented with 20 mM ANAP (free acid, AsisChem; Waltham, MA). Cells were incubated at 33 °C  
 432 and in the presence of 300  $\mu$ M tolbutamide to enhance protein expression and channel trafficking  
 433 to the plasma membrane (*Yan et al., 2007; Lin et al., 2015*). eRF1-E55D was included to increase  
 434 efficiency of ANAP incorporation (*Schmied et al., 2014*). Experiments were carried out 2-4 days  
 435 after transfection. We also expressed constructs labelled with ANAP at positions I182, F183, F198,  
 436 and I210. Kir6.2-F183\*, Kir6.2-F198\*, and Kir6.2-I210\* co-expressed with SUR1 did not produce  
 437 sufficient currents for subsequent experimentation. Mutations at I182 are known to produce pro-  
 438 found effects on nucleotide inhibition of K<sub>ATP</sub> (*Li et al., 2000*). Thus, we did not consider this site  
 439 for further experimentation.

#### 440 **Western blots.**

441 Transfected HEK-293T cells grown in 6-well plates were harvested in cold PBS (Life Technologies  
 442 Limited; Paisley, UK), pelleted at 0.2 x g for 2.5 minutes and resuspended in lysis buffer contain-  
 443 ing 0.5% Triton X-100, 100 mM potassium acetate, and a cOmplete protease inhibitor tablet (1  
 444 tablet/50 ml, Roche; Basel, Switzerland), buffered to pH 7.4. After a 30-minute benzonase (Sigma)  
 445 treatment at room temperature, samples were mixed with a DTT containing reducing agent and  
 446 loading buffer (NuPAGE, Invitrogen; Carlsbad, CA) and run on a precast Bis-Tris 4-12% poly-acrylamide  
 447 gel at 200 V for 40 minutes. Proteins were wet transferred overnight onto polyvinylidene diflu-  
 448 oride (PVDF) membranes (Immobilon P, Merck Millipore; Burlington, VT) in 25 mM Tris, 192 mM  
 449 glycine, 20% methanol, and 0.1% SDS at 10 V on ice. Membranes were blocked with 5% milk in  
 450 TBS-Tw (150 mM NaCl, 0.05% Tween 20, 25 mM mM Tris, pH 7.2) before staining for 30 minutes  
 451 with a 1:1000 dilution of rat anti-HA monoclonal antibody in TBS-Tw (clone 3F10, Roche). After  
 452 washing with TBS-Tw, membranes were incubated for 30 minutes with a 1:20,000 dilution of HRP-  
 453 conjugated goat anti-rat polyclonal antibodies in TBS-Tw (Jackson ImmunoResearch; Ely, UK). Detec-

454 tion was performed using the SuperSignal West Pico Chemiluminescent Substrate (Thermo Fisher)  
 455 and a C-DiGit Blot Scanner (Licor Biosciences; Lincoln, NE). Analysis was performed using custom  
 456 code written in Python.

457 To confirm our ability to express full-length Kir6.2\*-GFP, we performed western blots for HA-  
 458 tagged Kir6.2 constructs in detergent-solubilized HEK-293T cells (Figure 1—Figure supplement 1C).  
 459 The HA tag plus a short linker (YAYMEKGITDLAYPYDVPDY) was inserted in the extracellular region  
 460 following helix M1 of Kir6.2 between L100 and A101. Transfection of wild-type Kir6.2-HA or Kir6.2-  
 461 HA-GFP resulted in two bands on the western blots. The upper bands were close to the expected  
 462 sizes for full-length Kir6.2-HA and Kir6.2-HA-GFP (46 kDa and 77 kDa, respectively).

463 We consistently observed a lower molecular weight band as well. This band must correspond to  
 464 an N-terminally truncated Kir6.2 product, as the apparent molecular weight shifted with addition  
 465 of the C-terminal GFP tag. Based on the molecular weight, we predict that the truncated protein  
 466 product initiated from a start codon in the first transmembrane domain. Therefore, we believe  
 467 it is unlikely that this protein would form functional channels or traffic to the plasma membrane.  
 468 When Kir6.2-W311<sup>TAG</sup>-HA or Kir6.2-W311<sup>TAG</sup>-HA-GFP were co-transfected with SUR1, pANAP, and  
 469 eRF1-E55D, and cells were cultured in the presence of ANAP, the western blots were similar to wild-  
 470 type Kir6.2-HA or Kir6.2-HA-GFP. Over 90% full-length Kir6.2\*-HA-GFP was produced under these  
 471 conditions (Figure 1—Figure supplement 1D). We were unable to quantify the percentage of full-  
 472 length Kir6.2\*-HA produced as the C-terminally truncated band resulting from termination at the  
 473 TAG codon was very similar in size to the N-terminally truncated band. Co-expression with SUR1  
 474 increased the percentage of full-length Kir6.2\*-HA-GFP produced (Figure 1—Figure supplement  
 475 1D). In the absence of ANAP, we did not observe any full-length Kir6.2, indicating that there was no  
 476 read-through of the amber (TAG) stop codon (Figure 1—Figure supplement 1D).

#### 477 Confocal microscopy.

478 Confocal imaging was performed using a spinning-disk system (Ultra-VIEW VoX, PerkinElmer; Waltham,  
 479 MA) mounted on an IX81 microscope (Olympus; Southend-on-Sea, UK) with a Plan Apo 60x oil  
 480 immersion objective (NA = 1.4), provided by the Micron Advanced Bioimaging Unit, Oxford. Trans-  
 481 fected HEK-293T cells were incubated for 15 minutes with 1 nM CellMask Deep Red (Thermo Fisher)  
 482 to stain plasma membranes before washing with PBS and imaging. ANAP was excited with a solid-  
 483 state laser at 405 nm. GFP and CellMask were excited with an argon laser at 488 nm and 633 nm  
 484 respectively. Images were captured on an EMCCD camera (ImagEM; Hamamatsu Photonics; Wel-  
 485 wyn Garden City, UK) binned at 2 x 2 pixels and analysed using Python. A median filter with a  
 486 box size of 32 x 32 pixels was applied to improve the signal-to-noise ratio by reducing background  
 487 fluorescence.

488 We examined the surface expression of our ANAP-labelled constructs using confocal microscopy  
 489 (Figure 1—Figure supplement 1A,B). When Kir6.2-W311<sup>TAG</sup>-GFP was co-transfected with SUR1 along  
 490 with pANAP and eRF1-E55D in the presence of ANAP, the ANAP and GFP fluorescence were co-  
 491 localized at the plasma membrane. When wild-type Kir6.2-GFP was transfected under the same  
 492 conditions, only GFP fluorescence was observed at the plasma membrane. ANAP fluorescence  
 493 was diffuse and confined to the cytoplasm or intracellular structures. Thus, the plasma-membrane

494 ANAP signal was specific for Kir6.2\*-GFP.

495 **Surface expression assays.**

496 We measured surface expression of HA-tagged Kir6.2 subunits using an approach outlined by  
 497 Zerangue et al. (*Zerangue et al., 1999; Puljung et al., 2019*). Cells were plated on 19 mm cov-  
 498 erslips coated with poly-L-lysine and transfected as described above. Following incubation, cells  
 499 were rinsed with PBS before fixation with 10% formalin for 30 minutes at room temperature. Af-  
 500 ter washing again, cells were blocked with 1% BSA in PBS for 30 minutes at 4 °C before a 1-hour  
 501 incubation at 4 °C with a 1:1000 dilution (in PBS) of rat anti-HA monoclonal antibodies. Cells were  
 502 then washed 5 times on ice with 1% BSA in PBS followed by a 30-minute incubation at 4 °C with a  
 503 1:2000 dilution of HRP-conjugated goat anti-rat polyclonal antibodies. Cells were washed 5 times  
 504 in PBS + 1% BSA and 4 times in PBS. Coverslips were removed from the culture dishes and placed in  
 505 clean, untreated dishes for measurement. 300 µl of SuperSignal ELISA Femto Maximum Sensitivity  
 506 Substrate (Thermo Fisher) was added to each sample and the luminescence was measured using  
 507 a Glomax 20/20 Luminometer (Promega; Madison, WI) after a 10 second incubation.

508 HEK-293T cells were transfected with Kir6.2 constructs with or without a TAG stop codon cor-  
 509 responding to position 311. Cells were co-transfected with pANAP and eRF1-E55D in the presence  
 510 or absence of SUR1 and cultured with or without ANAP. Wild-type Kir6.2-HA and Kir6.2-HA-GFP in  
 511 the presence of SUR1 were included as positive controls. Kir6.2 constructs with no HA tag served  
 512 as negative controls. In the presence of ANAP, we observed strong trafficking of Kir6.2\*-HA-GFP to  
 513 the plasma membrane, but much less trafficking of Kir6.2\*-HA (Figure 1—Figure supplement 1E).  
 514 When cells were cultured in the absence of ANAP, we observed little to no Kir6.2 surface expression  
 515 from cells that were transfected with Kir6.2-W311<sup>TAG</sup>-HA or Kir6.2-W311<sup>TAG</sup>-HA-GFP, suggesting  
 516 that prematurely truncated constructs did not traffic to the plasma membrane. In the absence of  
 517 SUR1, surface expression was weak for both wild-type and tagged constructs, despite the reported  
 518 ability of Kir6.2-GFP to traffic to the plasma membrane in the absence of SUR1 (*John et al., 1998;*  
 519 *Makhina and Nichols, 1998*).

520 **Epifluorescence imaging and spectroscopy.**

521 Epifluorescence imaging and spectroscopy were performed using a Nikon Eclipse TE2000-U micro-  
 522 scope with a 60x water immersion objective (Plan Apo VC, NA = 1.2, Nikon; Kingston upon Thames,  
 523 UK) or a 100x oil immersion objective (Nikon, Apo TIRF, NA = 1.49). Imaging of ANAP was performed  
 524 using a 385 nm LED source (ThorLabs; Newton, NJ) with a 390/18 nm band-pass excitation filter, an  
 525 MD416 dichroic and a 479/40 nm band-pass emission filter (all from ThorLabs). GFP was imaged us-  
 526 ing a 490 nm LED source (ThorLabs) with a 480/40 nm band-pass excitation filter, a DM505 dichroic,  
 527 and a 510 nm long-pass emission filter (all from Chroma; Bellows Falls, VT). Fluorescence spectra  
 528 were collected by exciting ANAP as above but using a 400 nm long-pass emission filter (ThorLabs),  
 529 then passing emitted light through an IsoPlane 160 Spectrometer (Princeton Instruments; Tren-  
 530 ton, NJ) with a 300 g mm<sup>-1</sup> grating. Images were collected with 0.1 s to 1 s exposures on a Paxis  
 531 400BR\_eXcelon CCD (Princeton Instruments).

532 **Electrophysiology.**

533 Patch pipettes were pulled from thick-walled borosilicate glass capillaries (GC150F-15, Harvard Ap-  
 534 paratus; Holliston, MA) to a resistance of 1.5 MΩ to 2.5 MΩ when filled with pipette solution. Cur-  
 535 rents were recorded at –60 mV from excised inside-out patches using an Axopatch 200B amplifier  
 536 equipped with a Digidata 1322A digitizer and using pClamp 10 software (Molecular Devices; San  
 537 Jose, CA). Currents were low-pass filtered at 5 kHz and digitized at 20 kHz. The bath solution (intra-  
 538 cellular) contained 140 mM KCl, 10 mM HEPES, 1 mM EDTA and 1 mM EGTA (pH 7.3 with KOH). The  
 539 pipette solution (extracellular) contained 140 mM KCl, 10 mM HEPES and 1 mM EDTA (pH 7.4  
 540 with KOH). All experiments were carried out in Mg<sup>2+</sup>-free conditions. Currents were leak corrected  
 541 using the current remaining in bath solution containing 5 mM barium acetate at 60 mV, assuming  
 542 a linear leak with a reversal potential of 0 mV. Inhibition was calculated and corrected for run-  
 543 down by alternating test concentrations of nucleotide solution with nucleotide-free solution, then  
 544 expressing the test currents as a fraction of the average of the control currents before and after  
 545 the test solution as described previously (*Proks et al., 2010*).

546 **Unroofed binding measurements.**

547 Unroofed membranes were prepared as described previously (*Heuser, 2000; Zagotta et al., 2016;*  
*Puljung et al., 2019*). A coverslip plated with transfected HEK-293T cells was removed from the cul-  
 548 ture media and rinsed with PBS. The coverslip was then briefly sonicated using a probe sonicator  
 549 (Vibra-cell; Newtown, CT) leaving behind adherent plasma membrane fragments. Cells cultured on  
 550 FluoroDishes were rinsed and sonicated directly in the dish. Unroofed membrane fragments were  
 551 nearly invisible in bright-field images and identified by their GFP and ANAP fluorescence. Fluores-  
 552 cent TNP-nucleotides (Jena Bioscience; Jena, Germany) were diluted in bath solution and perfused  
 553 onto unroofed membranes using a valve controlled microvolume superfusion system (μFlow, ALA  
 554 Scientific Instruments; Farmingdale, NY).

556 Fluorescence spectra were collected as described above. A region of interest corresponding to  
 557 the membrane fragment was manually selected and line-averaged for each wavelength. A simi-  
 558 larly sized region of background was selected and averaged, then subtracted from the spectrum  
 559 of interest. After subtraction, ANAP intensity was calculated by averaging the fluorescence inten-  
 560 sity measured between 469.5 nm and 474.5 nm. Bleaching was corrected by fitting the normalised  
 561 ANAP intensity of exposures taken during perfusion with nucleotide-free solution to a single expo-  
 562 nential decay of the form

$$\frac{F}{F_{max}} = ae^{kt} + (1 - a) \quad (1)$$

563 then using the fit to correct the intensity of exposures taken during perfusion with test nucleotide  
 564 solutions.

565 For kinetic measurements, the solution changer and camera were controlled using pClamp  
 566 10 software coupled to a Digidata 1322A digitizer. Each fragment of unroofed membrane was  
 567 exposed three times to the same test concentration of nucleotide. Spectra were acquired every  
 568 three seconds. These technical replicates were averaged and presented as a single experiment.  
 569 Bleaching was corrected by fitting the ANAP intensity of the last ten spectra acquired during each

570 nucleotide-free solution wash to equation 1.

571 **Patch-clamp fluorometry.**

572 The tip of the patch pipette was centred on the slit of the spectrometer immediately after patch  
 573 excision. Currents were measured as described above. Fluorescence emission spectra from the  
 574 excised patch were acquired concurrently with current measurements, both during test solution  
 575 application as well as nucleotide-free solution. Background subtraction was slightly imperfect due  
 576 to the exclusion of TNP-ATP from volume of the glass of the pipette, resulting in spectra that have  
 577 negative intensities at the TNP-ATP peak at high nucleotide concentrations. However, this over-  
 578 subtraction does not affect the size of the ANAP peak, which we used to quantify nucleotide bind-  
 579 ing.

580 **Data processing and presentation.**

581 Raw spectrographic images and current traces were pre-processed in Python and Clampfit (Axon)  
 582 before analysis with R. Where applicable, all experimental data points are displayed in each fig-  
 583 ure. The number of experiments is reported in the figure legends and tables. To help visualise  
 584 uncertainty and prevent some data points being hidden, they are arranged with a small amount  
 585 of horizontal jitter; vertical position remains unaffected. Unless otherwise stated, summary statis-  
 586 tics are overlaid as the mean with error bars representing the standard error of the mean. Where  
 587 these error bars are not visible, they are smaller than the size of the point used for the mean.

588 Hill fits to fluorescence quenching were nonlinear least-squares fits to the following equation:

$$\frac{y}{y_{max}} = E_{max} + \frac{1 - E_{max}}{1 + 10^{(EC_{50} - [TNPATP])h}} \quad (2)$$

589 where  $y$  represents normalised fluorescence intensity and  $EC_{50}$  and  $[TNPATP]$  are  $\log_{10}$  values.  
 590 Current inhibition data were fit to the same equation but with  $y$  representing normalised current  
 591 magnitude,  $IC_{50}$  instead of  $EC_{50}$ , and  $I_{max}$  instead of  $E_{max}$ .

592  $k_{obs}$  values from single exponential fits with equation 1 to the wash-on and wash-off of TNP-ATP  
 593 in the time-course experiments were fit with the linear equation:

$$k_{obs} = k_{on}[TNPATP] + k_{off} \quad (3)$$

594 The gradient of the linear fit to the observed on-rate ( $k_{obs}$ ) is equivalent to  $k_{on}$ ;  $k_{off}$  is the intercept  
 595 at zero  $[TNPATP]$ . We also measured  $k_{off}$  directly from the dequenching of ANAP following TNP-  
 596 ATP wash-off. As expected, these values were independent of the  $[TNPATP]$  applied.

597 **Bayesian model fitting.**

598 The MWC-type models considered (Figure 2 and Figure 2—Figure Supplement 2) were formulated  
 599 as follows:

$$\frac{F}{F_{max}} = \frac{K_A[TNPATP](1 + K_A[TNPATP])^3 + LDK_A[TNPATP](1 + DK_A[TNPATP])^3}{(1 + K_A[TNPATP])^4 + L(1 + DK_A[TNPATP])^4} \quad (4)$$

$$\frac{\text{open channels}}{\text{total channels}} = \frac{L(1 + DK_A[TNPATP])^4}{(1 + K_A[TNPATP])^4 + L(1 + DK_A[TNPATP])^4} \quad (5)$$

600 When no ligand is present (i.e. when  $[TNPATP] = 0$ ), equation 5 becomes:

$$\frac{\text{open channels}}{\text{total channels}} = \frac{L}{1+L} \quad (6)$$

601 We can use this to normalise the predicted changes in the open fraction to an observed change  
602 in current as:

$$\frac{I}{I_{max}} = \frac{L(1 + DK_A[TNPATP])^4}{(1 + K_A[TNPATP])^4 + L(1 + DK_A[TNPATP])^4} \cdot \frac{1+L}{L} \quad (7)$$

603 Two variations on the full MWC model were also considered, and diagrammatic formulations  
604 are shown in Figure 2 - Figure supplement 1. The first was similar to the MWC-type model, except  
605 that the channels close after one molecule of TNP-ATP binding with subsequent binding events  
606 having no effect.

$$\frac{F}{F_{max}} = \frac{LDK_A[TNPATP](1 + 3K_A[TNPATP] + 3K_A^2[TNPATP]^2 + K_A^3[TNPATP]^3) + K_A[TNPATP](1 + K_A[TNPATP])^3}{L(1 + 4DK_A[TNPATP] + 6DK_A^2[TNPATP]^2 + 4DK_A^3[TNPATP]^3 + DK_A^4[TNPATP]^4) + (1 + K_A[TNPATP])^4} \quad (8)$$

$$\frac{I}{I_{max}} = \frac{L(1 + 4DK_A[TNPATP] + 6DK_A^2[TNPATP]^2 + 4DK_A^3[TNPATP]^3 + DK_A^4[TNPATP]^4) + (1 + K_A[TNPATP])^4}{L(1 + 4DK_A[TNPATP] + 6DK_A^2[TNPATP]^2 + 4DK_A^3[TNPATP]^3 + DK_A^4[TNPATP]^4) + (1 + K_A[TNPATP])^4} \cdot \frac{1+L}{L} \quad (9)$$

607 The second alternate model was the same as the full MWC model, but with an additional term  
608 C describing binding cooperativity between Kir6.2 subunits.

$$\frac{F}{F_{max}} = \frac{LDK_A[TNPATP](1 + 3CDK_A[TNPATP] + 3C^2D^2K_A^2[TNPATP]^2 + C^3D^3K_A^3[TNPATP]^3 + K_A[TNPATP](1 + 3CK_A[TNPATP] + 3C^2K_A^2[TNPATP]^2 + C^3K_A^3[TNPATP]^3)}{L(1 + 4DK_A[TNPATP] + 6CD^2K_A^2[TNPATP]^2 + 4C^2D^3K_A^3[TNPATP]^3 + C^3D^4K_A^4[TNPATP]^4 + 1 + 4K_A[TNPATP] + 6CK_A^2[TNPATP]^2 + 4C^2K_A^3[TNPATP]^3 + C^3K_A^4[TNPATP]^4)} \quad (10)$$

$$\frac{I}{I_{max}} = \frac{L(1 + 4DK_A[TNPATP] + 6CD^2K_A^2[TNPATP]^2 + 4C^2D^3K_A^3[TNPATP]^3 + C^3D^4K_A^4[TNPATP]^4) + (1 + 4K_A[TNPATP] + 6CK_A^2[TNPATP]^2 + 4C^2K_A^3[TNPATP]^3 + C^3K_A^4[TNPATP]^4)}{L(1 + 4DK_A[TNPATP] + 6CD^2K_A^2[TNPATP]^2 + 4C^2D^3K_A^3[TNPATP]^3 + C^3D^4K_A^4[TNPATP]^4) + (1 + 4K_A[TNPATP] + 6CK_A^2[TNPATP]^2 + 4C^2K_A^3[TNPATP]^3 + C^3K_A^4[TNPATP]^4)} \cdot \frac{1+L}{L} \quad (11)$$

609 Each model was fit to the combined patch-clamp fluorometry datasets using the brms package  
610 (*Gelman et al., 2015; Burkner, 2017*) in R. Prior probability distributions for each parameter were  
611 supplied as:

$$\log_{10}(L) \sim \text{Normal}(\mu : 0, \sigma^2 : 0.7)$$

$$D \sim \text{Uniform}(\text{min} : 0, \text{max} : 1)$$

$$\log_{10}(K_A) \sim \text{Uniform}(\text{min} : 2, \text{max} : 6)$$

$$C \sim \text{Uniform}(\text{min} : 0, \text{max} : 1)$$

612 so that all priors are flat apart from L, which is weakly informative with 99% of its density falling  
613 between unliganded open probabilities of 0.01 and 0.99, and 85% falling between 0.1 and 0.9.

614 Each model was run with 4 independent chains for 10,000 iterations each after a burn-in period

of 20,000 iterations, saving every 10th sample for a total of 4,000 samples per model. Each model parameter achieved a minimum effective sample size of 3,500 and a potential scale reduction statistic ( $\hat{R}$ ) of 1.00. Where applicable, the posterior probabilities of each parameter are reported as the median and the 95% equal-tailed interval. Bayes factors were calculated using bridge-sampling (Gronau et al., 2017), and leave-one-out cross-validation (LOO-CV) was performed using the loo package (Vehtari et al., 2017).

### 621 Docking.

Computational docking of TNP-ATP into the nucleotide binding site of Kir6.2 was performed using AutoDock-Vina (?) and Pymol (Schrödinger, LLC; New York, NY). 11 TNP-ATP structures from the Protein Data Bank (PDB accession #s 1I5D, 3AR7, 5NCQ, 5SVQ, 5XW6, 2GVD, 5A3S, 2PMK, and 3B5J) were used as starting poses and a 15x11.25x15 Å box was centred on the ATP bound to Kir6.2 in PDB accession #6BAA (Martin et al., 2017). Protonation states for each residue were assigned using PDB2PQR and PROPKA 3.0 (Dolinsky et al., 2004). The modal highest-scoring pose from the docking run was selected (PDB accession #5XW6, Kasuya et al. (2017)) and distances were measured from a pseudo atom at the centre of the fluorescent moiety. TNP-ATP (PDB #3AR7, Toyoshima et al. (2011)) was positioned into the first nucleotide binding domain of SUR1 (PDB #6PZI, Martin et al. (2019)) using the alignment tool in Pymol.

### 632 Chemicals and stock solutions.

Unless otherwise noted, all chemicals were obtained from Sigma. TNP-ATP was obtained as a 10 mM aqueous stock from Jena Bioscience and stored at -20 °C. 1 mM aqueous stocks of ANAP-TFA were prepared by dissolving the free acid in 30 mM NaOH, and were stored at -20 °C. Tolbutamide stocks (50 mM) were prepared in 100 mM KOH and stored at -20 °C.

### 637 Acknowledgments

We wish to thank Raul Terron Exposito for technical assistance and Dr. Natascia Vedovato for helpful discussions. James Cantley provided access to the Licor scanner for western blots. This work was supported by the Biotechnology and Biological Science Research Council (BB/R002517/1) and the Wellcome Trust Oxion graduate program.

### 642 References

- 643 Aguilar-Bryan L, Nichols CG, Wechsler SW, Clement JP, Boyd r A E, Gonzalez G, Herrera-Sosa H, Nguy K, Bryan J, Nelson DA. Cloning of the beta cell high-affinity sulfonylurea receptor: a regulator of insulin secretion. Science. 1995; 268(5209):423–6. [HTTPS://WWW.NCBI.NLM.NIH.GOV/PUBMED/7716547.](https://www.ncbi.nlm.nih.gov/pmc/articles/PMC7716547/)
- 646 Ashcroft FM, Puljung MC, Vedovato N. Neonatal Diabetes and the KATP Channel: From Mutation to Therapy. Trends Endocrinol Metab. 2017; 28(5):377–387. [HTTPS://WWW.NCBI.NLM.NIH.GOV/PUBMED/28262438](https://www.ncbi.nlm.nih.gov/pmc/articles/PMC28262438/), doi: 10.1016/j.tem.2017.02.003.
- 649 Ashcroft FM, Rorsman P. K(ATP) channels and islet hormone secretion: new insights and controversies. Nat Rev Endocrinol. 2013; 9(11):660–9. [HTTPS://WWW.NCBI.NLM.NIH.GOV/PUBMED/24042324](https://www.ncbi.nlm.nih.gov/pmc/articles/PMC24042324/), doi: 10.1038/nrendo.2013.166.

- 652 Babenko AP, Bryan J. Sur domains that associate with and gate KATP pores define a novel gate-  
 653 keeper. *J Biol Chem.* 2003; 278(43):41577–80. [HTTPS://WWW.NCBI.NLM.NIH.GOV/PUBMED/12941953](https://www.ncbi.nlm.nih.gov/PUBMED/12941953), doi:  
 654 10.1074/jbc.C300363200.
- 655 Biskup C, Kusch J, Schulz E, Nache V, Schwede F, Lehmann F, Hagen V, Benndorf K. Relating ligand binding  
 656 to activation gating in CNGA2 channels. *Nature.* 2007; 446(7134):440–3. [HTTPS://WWW.NCBI.NLM.NIH.GOV/PUBMED/17322905](https://www.ncbi.nlm.nih.gov/PUBMED/17322905), doi: 10.1038/nature05596.
- 658 Burkner PC. brms: An R Package for Bayesian Multilevel Models Using Stan. *Journal of Statistical Software.*  
 659 2017; 80(1):1–28. <[Goto ISI](#)>://WOS:000408409900001.
- 660 Chan KW, Zhang H, Logothetis DE. N-terminal transmembrane domain of the SUR controls trafficking and  
 661 gating of Kir6 channel subunits. *EMBO J.* 2003; 22(15):3833–43. [HTTPS://WWW.NCBI.NLM.NIH.GOV/PUBMED/12881418](https://www.ncbi.nlm.nih.gov/PUBMED/12881418), doi: 10.1093/emboj/cdg376.
- 663 Chatterjee A, Guo J, Lee HS, Schultz PG. A genetically encoded fluorescent probe in mammalian  
 664 cells. *J Am Chem Soc.* 2013; 135(34):12540–3. [HTTPS://WWW.NCBI.NLM.NIH.GOV/PUBMED/23924161](https://www.ncbi.nlm.nih.gov/PUBMED/23924161), doi:  
 665 10.1021/ja4059553.
- 666 Craig TJ, Ashcroft FM, Proks P. How ATP inhibits the open K(ATP) channel. *J Gen Physiol.* 2008; 132(1):131–44.  
 667 [HTTPS://WWW.NCBI.NLM.NIH.GOV/PUBMED/18591420](https://www.ncbi.nlm.nih.gov/PUBMED/18591420), doi: 10.1085/jgp.200709874.
- 668 Dolinsky TJ, Nielsen JE, McCammon JA, Baker NA. PDB2PQR: an automated pipeline for the setup of Poisson-  
 669 Boltzmann electrostatics calculations. *Nucleic Acids Res.* 2004; 32(Web Server issue):W665–7. [HTTPS://WWW.NCBI.NLM.NIH.GOV/PUBMED/15215472](https://www.ncbi.nlm.nih.gov/PUBMED/15215472), doi: 10.1093/nar/gkh381.
- 671 Drain P, Geng X, Li L. Concerted gating mechanism underlying KATP channel inhibition by ATP. *Biophys J.* 2004;  
 672 86(4):2101–12. [HTTPS://WWW.NCBI.NLM.NIH.GOV/PUBMED/15041650](https://www.ncbi.nlm.nih.gov/PUBMED/15041650), doi: 10.1016/S0006-3495(04)74269-1.
- 673 Drain P, Li L, Wang J. KATP channel inhibition by ATP requires distinct functional domains of the cytoplasmic C  
 674 terminus of the pore-forming subunit. *Proc Natl Acad Sci U S A.* 1998; 95(23):13953–8. [HTTPS://WWW.NCBI.NLM.NIH.GOV/PUBMED/9811907](https://www.ncbi.nlm.nih.gov/PUBMED/9811907).
- 676 Enkvetchakul D, Loussouarn G, Makhina E, Shyng SL, Nichols CG. The kinetic and physical basis of K(ATP)  
 677 channel gating: toward a unified molecular understanding. *Biophys J.* 2000; 78(5):2334–48. [HTTPS://WWW.NCBI.NLM.NIH.GOV/PUBMED/10777731](https://www.ncbi.nlm.nih.gov/PUBMED/10777731), doi: 10.1016/S0006-3495(00)76779-8.
- 679 Enkvetchakul D, Nichols CG. Gating mechanism of KATP channels: function fits form. *J Gen Physiol.* 2003;  
 680 122(5):471–80. [HTTPS://WWW.NCBI.NLM.NIH.GOV/PUBMED/14581579](https://www.ncbi.nlm.nih.gov/PUBMED/14581579), doi: 10.1085/jgp.200308878.
- 681 Fang K, Csanady L, Chan KW. The N-terminal transmembrane domain (TMD0) and a cytosolic linker (L0) of  
 682 sulphonylurea receptor define the unique intrinsic gating of KATP channels. *J Physiol.* 2006; 576(Pt 2):379–  
 683 89. [HTTPS://WWW.NCBI.NLM.NIH.GOV/PUBMED/16887879](https://www.ncbi.nlm.nih.gov/PUBMED/16887879), doi: 10.1113/jphysiol.2006.112748.
- 684 Flanagan SE, Edghill EL, Gloyn AL, Ellard S, Hattersley AT. Mutations in KCNJ11, which encodes Kir6.2, are a com-  
 685 mon cause of diabetes diagnosed in the first 6 months of life, with the phenotype determined by genotype. *Di-  
 686 abetologia.* 2006; 49(6):1190–7. [HTTPS://WWW.NCBI.NLM.NIH.GOV/PUBMED/16609879](https://www.ncbi.nlm.nih.gov/PUBMED/16609879), doi: 10.1007/s00125-  
 687 006-0246-z.
- 688 Gelman A, Lee D, Guo JQ. Stan: A Probabilistic Programming Language for Bayesian Inference and Op-  
 689 timization. *Journal of Educational and Behavioral Statistics.* 2015; 40(5):530–543. <[Goto ISI](#)>://WOS:  
 690 000363883900006.
- 691 Gloyn AL, Diatloff-Zito C, Edghill EL, Bellanne-Chantelot C, Nivot S, Coutant R, Ellard S, Hattersley AT, Robert  
 692 JJ. KCNJ11 activating mutations are associated with developmental delay, epilepsy and neonatal diabetes  
 693 syndrome and other neurological features. *Eur J Hum Genet.* 2006; 14(7):824–30. [HTTPS://WWW.NCBI.NLM.NIH.GOV/PUBMED/16670688](https://www.ncbi.nlm.nih.gov/PUBMED/16670688), doi: 10.1038/sj.ejhg.5201629.

- 695 **Gribble FM**, Tucker SJ, Haug T, Ashcroft FM. MgATP activates the beta cell KATP channel by interaction with its  
 696 SUR1 subunit. *Proc Natl Acad Sci U S A.* 1998; 95(12):7185–90. [HTTPS://WWW.NCBI.NLM.NIH.GOV/PUBMED/9618560](https://www.ncbi.nlm.nih.gov/pmc/articles/PMC1560/), doi: 10.1073/pnas.95.12.7185.
- 698 **Gronau QF**, Singmann H, Wagenmakers EJ. bridgesampling: An R Package for Estimating Normalizing Con-  
 699 stants. arXiv e-prints. 2017 Oct; p. arXiv:1710.08162.
- 700 **Heuser J.** The production of 'cell cortices' for light and electron microscopy. *Traffic.* 2000; 1(7):545–52. [HTTPS://WWW.NCBI.NLM.NIH.GOV/PUBMED/11208142](https://www.ncbi.nlm.nih.gov/pmc/articles/PMC1208142/).
- 702 **Hines KE**, Middendorf TR, Aldrich RW. Determination of parameter identifiability in nonlinear biophysical mod-  
 703 els: A Bayesian approach. *J Gen Physiol.* 2014; 143(3):401–16. [HTTPS://WWW.NCBI.NLM.NIH.GOV/PUBMED/24516188](https://www.ncbi.nlm.nih.gov/pmc/articles/PMC42516188/), doi: 10.1085/jgp.201311116.
- 705 **Inagaki N**, Gono T, Clement JP, Namba N, Inazawa J, Gonzalez G, Aguilar-Bryan L, Seino S, Bryan J. Reconstitu-  
 706 tion of IKATP: an inward rectifier subunit plus the sulfonylurea receptor. *Science.* 1995; 270(5239):1166–70.  
 707 [HTTPS://WWW.NCBI.NLM.NIH.GOV/PUBMED/7502040](https://www.ncbi.nlm.nih.gov/pmc/articles/PMC7502040/).
- 708 **Inagaki N**, Gono T, Seino S. Subunit stoichiometry of the pancreatic beta-cell ATP-sensitive K<sup>+</sup> channel. *FEBS*  
 709 *Lett.* 1997; 409(2):232–6. [HTTPS://WWW.NCBI.NLM.NIH.GOV/PUBMED/9202152](https://www.ncbi.nlm.nih.gov/pmc/articles/PMC9202152/).
- 710 **John SA**, Monck JR, Weiss JN, Ribalet B. The sulphonylurea receptor SUR1 regulates ATP-sensitive mouse  
 711 Kir6.2 K<sup>+</sup> channels linked to the green fluorescent protein in human embryonic kidney cells (HEK 293). *J*  
 712 *Physiol.* 1998; 510 ( Pt 2):333–45. [HTTPS://WWW.NCBI.NLM.NIH.GOV/PUBMED/9705987](https://www.ncbi.nlm.nih.gov/pmc/articles/PMC9705987/), doi: 10.1111/j.1469-  
 713 7793.1998.333bk.x.
- 714 **Kasuya G**, Yamaura T, Ma XB, Nakamura R, Takemoto M, Nagumo H, Tanaka E, Dohmae N, Nakane T, Yu Y, Ishi-  
 715 tani R, Matsuzaki O, Hattori M, Nureki O. Structural insights into the competitive inhibition of the ATP-gated  
 716 P2X receptor channel. *Nat Commun.* 2017; 8(1):876. [HTTPS://WWW.NCBI.NLM.NIH.GOV/PUBMED/29026074](https://www.ncbi.nlm.nih.gov/pmc/articles/PMC29026074/),  
 717 doi: 10.1038/s41467-017-00887-9.
- 718 **Kusch J**, Biskup C, Thon S, Schulz E, Nache V, Zimmer T, Schwede F, Benndorf K. Interdependence of receptor  
 719 activation and ligand binding in HCN2 pacemaker channels. *Neuron.* 2010; 67(1):75–85. [HTTPS://WWW.NCBI.NLM.NIH.GOV/PUBMED/20624593](https://www.ncbi.nlm.nih.gov/pmc/articles/PMC20624593/), doi: 10.1016/j.neuron.2010.05.022.
- 721 **Li L**, Wang J, Drain P. The I182 region of k(ir)6.2 is closely associated with ligand binding in K(ATP) channel  
 722 inhibition by ATP. *Biophys J.* 2000; 79(2):841–52. [HTTPS://WWW.NCBI.NLM.NIH.GOV/PUBMED/10920016](https://www.ncbi.nlm.nih.gov/pmc/articles/PMC10920016/), doi:  
 723 10.1016/S0006-3495(00)76340-5.
- 724 **Lin CY**, Huang Z, Wen W, Wu A, Wang C, Niu L. Enhancing Protein Expression in HEK-293 Cells by Lowering Cul-  
 725 ture Temperature. *PLoS One.* 2015; 10(4):e0123562. [HTTPS://WWW.NCBI.NLM.NIH.GOV/PUBMED/2589327](https://www.ncbi.nlm.nih.gov/pmc/articles/PMC4589327/),  
 726 doi: 10.1371/journal.pone.0123562.
- 727 **Makhina EN**, Nichols CG. Independent trafficking of KATP channel subunits to the plasma membrane. *J Biol*  
 728 *Chem.* 1998; 273(6):3369–74. [HTTPS://WWW.NCBI.NLM.NIH.GOV/PUBMED/9452456](https://www.ncbi.nlm.nih.gov/pmc/articles/PMC9452456/).
- 729 **Markworth E**, Schwanstecher C, Schwanstecher M. ATP4- mediates closure of pancreatic beta-cell ATP-  
 730 sensitive potassium channels by interaction with 1 of 4 identical sites. *Diabetes.* 2000; 49(9):1413–8. [HTTPS://WWW.NCBI.NLM.NIH.GOV/PUBMED/10969823](https://www.ncbi.nlm.nih.gov/pmc/articles/PMC10969823/), doi: 10.2337/diabetes.49.9.1413.
- 732 **Martin GM**, Kandasamy B, DiMaio F, Yoshioka C, Shyng SL. Anti-diabetic drug binding site in a mammalian  
 733 KATP channel revealed by Cryo-EM. *Elife.* 2017; 6. [HTTPS://WWW.NCBI.NLM.NIH.GOV/PUBMED/29035201](https://www.ncbi.nlm.nih.gov/pmc/articles/PMC29035201/), doi:  
 734 10.7554/eLife.31054.

- 735    **Martin GM**, Sung MW, Yang Z, Innes LM, Kandasamy B, David LL, Yoshioka C, Shyng SL. Mechanism of pharma-  
 736    cochaperoning in a mammalian KATP channel revealed by cryo-EM. *Elife*. 2019; 8. [HTTPS://WWW.NCBI.NLM.NIH.GOV/PUBMED/31343405](https://www.ncbi.nlm.nih.gov/pmc/articles/3134340/), doi: 10.7554/elife.46417.
- 738    **Masia R**, Koster JC, Tumini S, Chiarelli F, Colombo C, Nichols CG, Barbetti F. An ATP-binding mutation  
 739    (G334D) in KCNJ11 is associated with a sulfonylurea-insensitive form of developmental delay, epilepsy, and  
 740    neonatal diabetes. *Diabetes*. 2007; 56(2):328–36. [HTTPS://WWW.NCBI.NLM.NIH.GOV/PUBMED/17259376](https://www.ncbi.nlm.nih.gov/pmc/articles/1725937/), doi:  
 741    10.2337/db06-1275.
- 742    **McTaggart JS**, Clark RH, Ashcroft FM. The role of the KATP channel in glucose homeostasis in health and  
 743    disease: more than meets the islet. *J Physiol*. 2010; 588(Pt 17):3201–9. [HTTPS://WWW.NCBI.NLM.NIH.GOV/PUBMED/20519313](https://www.ncbi.nlm.nih.gov/pmc/articles/20519313/), doi: 10.1113/jphysiol.2010.191767.
- 745    **Monod J**, Wyman J, Changeux JP. On the Nature of Allosteric Transitions: A Plausible Model. *J Mol Biol*. 1965;  
 746    12:88–118. [HTTPS://WWW.NCBI.NLM.NIH.GOV/PUBMED/14343300](https://www.ncbi.nlm.nih.gov/pmc/articles/14343300/).
- 747    **Nichols CG**, Shyng SL, Nestorowicz A, Glaser B, Clement JP, Gonzalez G, Aguilar-Bryan L, Permutt MA, Bryan  
 748    J. Adenosine diphosphate as an intracellular regulator of insulin secretion. *Science*. 1996; 272(5269):1785–7.  
 749    [HTTPS://WWW.NCBI.NLM.NIH.GOV/PUBMED/8650576](https://www.ncbi.nlm.nih.gov/pmc/articles/8650576/).
- 750    **Pratt EB**, Zhou Q, Gay JW, Shyng SL. Engineered interaction between SUR1 and Kir6.2 that enhances ATP  
 751    sensitivity in KATP channels. *J Gen Physiol*. 2012; 140(2):175–87. [HTTPS://WWW.NCBI.NLM.NIH.GOV/PUBMED/22802363](https://www.ncbi.nlm.nih.gov/pmc/articles/22802363/), doi: 10.1085/jgp.201210803.
- 753    **Proks P**, Puljung MC, Vedovato N, Sachse G, Mulvaney R, Ashcroft FM. Running out of time: the de-  
 754    cline of channel activity and nucleotide activation in adenosine triphosphate-sensitive K-channels. *Philos  
 755    Trans R Soc Lond B Biol Sci*. 2016; 371(1700). [HTTPS://WWW.NCBI.NLM.NIH.GOV/PUBMED/27377720](https://www.ncbi.nlm.nih.gov/pmc/articles/27377720/), doi:  
 756    10.1098/rstb.2015.0426.
- 757    **Proks P**, de Wet H, Ashcroft FM. Activation of the K(ATP) channel by Mg-nucleotide interaction with  
 758    SUR1. *J Gen Physiol*. 2010; 136(4):389–405. [HTTPS://WWW.NCBI.NLM.NIH.GOV/PUBMED/20876358](https://www.ncbi.nlm.nih.gov/pmc/articles/20876358/), doi:  
 759    10.1085/jgp.201010475.
- 760    **Puljung M**, Vedovato N, Usher S, Ashcroft F. Activation mechanism of ATP-sensitive K(+) channels explored  
 761    with real-time nucleotide binding. *Elife*. 2019; 8. [HTTPS://WWW.NCBI.NLM.NIH.GOV/PUBMED/30789344](https://www.ncbi.nlm.nih.gov/pmc/articles/30789344/), doi:  
 762    10.7554/elife.41103.
- 763    **Puljung MC**. Cryo-electron microscopy structures and progress toward a dynamic understanding of KATP  
 764    channels. *J Gen Physiol*. 2018; 150(5):653–669. [HTTPS://WWW.NCBI.NLM.NIH.GOV/PUBMED/29685928](https://www.ncbi.nlm.nih.gov/pmc/articles/29685928/), doi:  
 765    10.1085/jgp.201711978.
- 766    **Quan Y**, Barszczuk A, Feng ZP, Sun HS. Current understanding of K ATP channels in neonatal diseases: focus  
 767    on insulin secretion disorders. *Acta Pharmacol Sin*. 2011; 32(6):765–80. [HTTPS://WWW.NCBI.NLM.NIH.GOV/PUBMED/21602835](https://www.ncbi.nlm.nih.gov/pmc/articles/21602835/), doi: 10.1038/aps.2011.57.
- 769    **Ribalet B**, John SA, Xie LH, Weiss JN. ATP-sensitive K<sup>+</sup> channels: regulation of bursting by the sulphonylurea  
 770    receptor, PIP2 and regions of Kir6.2. *J Physiol*. 2006; 571(Pt 2):303–17. [HTTPS://WWW.NCBI.NLM.NIH.GOV/PUBMED/16373383](https://www.ncbi.nlm.nih.gov/pmc/articles/16373383/), doi: 10.1113/jphysiol.2005.100719.
- 772    **Sakura H**, Ammala C, Smith PA, Gribble FM, Ashcroft FM. Cloning and functional expression of the cDNA  
 773    encoding a novel ATP-sensitive potassium channel subunit expressed in pancreatic beta-cells, brain, heart  
 774    and skeletal muscle. *FEBS Lett*. 1995; 377(3):338–44. [HTTPS://WWW.NCBI.NLM.NIH.GOV/PUBMED/8549751](https://www.ncbi.nlm.nih.gov/pmc/articles/8549751/),  
 775    doi: 10.1016/0014-5793(95)01369-5.

- 776 Schmied WH, Elsasser SJ, Uttamapinant C, Chin JW. Efficient multisite unnatural amino acid incorpo-  
 777 ration in mammalian cells via optimized pyrrolysyl tRNA synthetase/tRNA expression and engineered  
 778 eRF1. *J Am Chem Soc.* 2014; 136(44):15577–83. [HTTPS://WWW.NCBI.NLM.NIH.GOV/PUBMED/25350841](https://www.ncbi.nlm.nih.gov/pmc/articles/PMC2535084/), doi:  
 779 10.1021/ja5069728.
- 780 Snider KE, Becker S, Boyajian L, Shyng SL, MacMullen C, Hughes N, Ganapathy K, Bhatti T, Stanley CA, Ganguly  
 781 A. Genotype and phenotype correlations in 417 children with congenital hyperinsulinism. *J Clin Endocrinol*  
 782 *Metab.* 2013; 98(2):E355–63. [HTTPS://WWW.NCBI.NLM.NIH.GOV/PUBMED/23275527](https://www.ncbi.nlm.nih.gov/pmc/articles/PMC3275527/), doi: 10.1210/jc.2012-  
 783 2169.
- 784 Toyoshima C, Yonekura S, Tsueda J, Iwasawa S. Trinitrophenyl derivatives bind differently from parent adenine  
 785 nucleotides to Ca<sup>2+</sup>-ATPase in the absence of Ca<sup>2+</sup>. *Proc Natl Acad Sci U S A.* 2011; 108(5):1833–8. [HTTPS://WWW.NCBI.NLM.NIH.GOV/PUBMED/21239683](https://www.ncbi.nlm.nih.gov/pmc/articles/PMC31239683/), doi: 10.1073/pnas.1017659108.
- 787 Trapp S, Proks P, Tucker SJ, Ashcroft FM. Molecular analysis of ATP-sensitive K channel gating and implications  
 788 for channel inhibition by ATP. *J Gen Physiol.* 1998; 112(3):333–49. [HTTPS://WWW.NCBI.NLM.NIH.GOV/PUBMED/9725893](https://www.ncbi.nlm.nih.gov/pmc/articles/PMC9725893/), doi: 10.1085/jgp.112.3.333.
- 790 Tucker SJ, Gribble FM, Zhao C, Trapp S, Ashcroft FM. Truncation of Kir6.2 produces ATP-sensitive K<sup>+</sup> channels  
 791 in the absence of the sulphonylurea receptor. *Nature.* 1997; 387(6629):179–83. [HTTPS://WWW.NCBI.NLM.NIH.GOV/PUBMED/9144288](https://www.ncbi.nlm.nih.gov/pmc/articles/PMC9144288/), doi: 10.1038/387179a0.
- 793 Tusnady GE, Bakos E, Varadi A, Sarkadi B. Membrane topology distinguishes a subfamily of the ATP-binding cas-  
 794 sette (ABC) transporters. *FEBS Lett.* 1997; 402(1):1–3. [HTTPS://WWW.NCBI.NLM.NIH.GOV/PUBMED/9013845](https://www.ncbi.nlm.nih.gov/pmc/articles/PMC9013845/),  
 795 doi: 10.1016/s0014-5793(96)01478-0.
- 796 Ueda K, Komine J, Matsuo M, Seino S, Amachi T. Cooperative binding of ATP and MgADP in the sulfonylurea  
 797 receptor is modulated by glibenclamide. *Proc Natl Acad Sci U S A.* 1999; 96(4):1268–72. [HTTPS://WWW.NCBI.NLM.NIH.GOV/PUBMED/9990013](https://www.ncbi.nlm.nih.gov/pmc/articles/PMC9990013/).
- 799 Vedovato N, Ashcroft FM, Puljung MC. The Nucleotide-Binding Sites of SUR1: A Mechanistic  
 800 Model. *Biophys J.* 2015; 109(12):2452–60. [HTTPS://WWW.NCBI.NLM.NIH.GOV/PUBMED/26682803](https://www.ncbi.nlm.nih.gov/pmc/articles/PMC46682803/), doi:  
 801 10.1016/j.bpj.2015.10.026.
- 802 Vehtari A, Gelman A, Gabry J. Practical Bayesian model evaluation using leave-one-out cross-validation and  
 803 WAIC (vol 27, pg 1413, 2017). *Statistics and Computing.* 2017; 27(5):1433–1433. <Go to ISI>://WOS:  
 804 000400831700018, doi: 10.1007/s11222-016-9709-3.
- 805 Wagenmakers EJ. A practical solution to the pervasive problems of p values. *Psychon Bull Rev.* 2007; 14(5):779–  
 806 804. [HTTPS://WWW.NCBI.NLM.NIH.GOV/PUBMED/18087943](https://www.ncbi.nlm.nih.gov/pmc/articles/PMC18087943/).
- 807 Wang R, Zhang X, Cui N, Wu J, Piao H, Wang X, Su J, Jiang C. Subunit-stoichiometric evidence for kir6.2 channel  
 808 gating, ATP binding, and binding-gating coupling. *Mol Pharmacol.* 2007; 71(6):1646–56. [HTTPS://WWW.NCBI.NLM.NIH.GOV/PUBMED/17369308](https://www.ncbi.nlm.nih.gov/pmc/articles/PMC17369308/), doi: 10.1124/mol.106.030528.
- 810 Wu S, Vysotskaya ZV, Xu X, Xie C, Liu Q, Zhou L. State-dependent cAMP binding to functioning HCN channels  
 811 studied by patch-clamp fluorometry. *Biophys J.* 2011; 100(5):1226–32. [HTTPS://WWW.NCBI.NLM.NIH.GOV/PUBMED/21354395](https://www.ncbi.nlm.nih.gov/pmc/articles/PMC31354395/), doi: 10.1016/j.bpj.2011.01.034.
- 813 Yan FF, Lin YW, MacMullen C, Ganguly A, Stanley CA, Shyng SL. Congenital hyperinsulinism associated ABCC8  
 814 mutations that cause defective trafficking of ATP-sensitive K<sup>+</sup> channels: identification and rescue. *Diabetes.*  
 815 2007; 56(9):2339–48. [HTTPS://WWW.NCBI.NLM.NIH.GOV/PUBMED/17575084](https://www.ncbi.nlm.nih.gov/pmc/articles/PMC17575084/), doi: 10.2337/db07-0150.
- 816 Zagotta WN, Gordon MT, Senning EN, Munari MA, Gordon SE. Measuring distances between TRPV1 and the  
 817 plasma membrane using a noncanonical amino acid and transition metal ion FRET. *J Gen Physiol.* 2016;  
 818 147(2):201–16. [HTTPS://WWW.NCBI.NLM.NIH.GOV/PUBMED/26755770](https://www.ncbi.nlm.nih.gov/pmc/articles/PMC496755770/), doi: 10.1085/jgp.201511531.

- 819 Zerangue N, Schwappach B, Jan YN, Jan LY. A new ER trafficking signal regulates the subunit stoichiometry of plasma membrane K(ATP) channels. *Neuron*. 1999; 22(3):537–48. [HTTPS://WWW.NCBI.NLM.NIH.GOV/PUBMED/10197533](https://www.ncbi.nlm.nih.gov/pmc/articles/PMC1999001/).
- 820  
821  
822 Zheng J, Zagotta WN. Patch-clamp fluorometry recording of conformational rearrangements of ion channels. *Sci STKE*. 2003; 2003(176):PL7. [HTTPS://WWW.NCBI.NLM.NIH.GOV/PUBMED/12671191](https://www.ncbi.nlm.nih.gov/pmc/articles/PMC1999001/), doi: 10.1126/stke.2003.176.pl7.
- 823  
824

Fluorescence Quenching	Construct	Term	Estimate	Standard Error
TNP-ATP n = 18	Kir6.2*-GFP+SUR1	$EC_{50}$	-4.59	0.05
		$h$	0.82	0.05
		$E_{max}$	0.93	0.03
Kir6.2*-G334D-GFP+SUR1 n = 9	Kir6.2*-G334D-GFP+SUR1	$EC_{50}$	-3.31	2.23
		$h$	2.63	17.70
		$E_{max}$	0.08	0.26
Kir6.2*-C166S-GFP+SUR1 n = 12	Kir6.2*-C166S-GFP+SUR1	$EC_{50}$	-4.50	0.05
		$h$	0.92	0.08
		$E_{max}$	0.87	0.03
Kir6.2*-GFP n = 14	Kir6.2*-GFP	$EC_{50}$	-4.42	0.05
		$h$	0.83	0.05
		$E_{max}$	0.92	0.03

**Table 1. Table 1: Hill fit parameters from unroofed membranes.**  $EC_{50}$  values and their standard errors are reported in  $\log_{10} M^{-1}$ .

---

## 825 Tables and supplementary figures

Current Inhibition	Construct	Term	Estimate	Standard Error
ATP	Kir6.2-GFP+SUR1 n = 3	$IC_{50}$	-4.20	0.07
		$h$	1.28	0.21
		$I_{max}$	0.99	0.06
ATP	Kir6.2-GFP n = 2	$IC_{50}$	-3.31	0.05
		$h$	1.15	0.12
		$I_{max}$	0.93	0.03
ATP	Kir6.2*-GFP+SUR1 n = 4	$IC_{50}$	-4.10	0.06
		$h$	1.42	0.21
		$I_{max}$	1.00	0.05
TNP-ATP	Kir6.2-GFP+SUR1 n = 7	$IC_{50}$	-5.93	0.04
		$h$	1.14	0.11
		$I_{max}$	0.97	0.02
TNP-ATP	Kir6.2-GFP n = 3	$IC_{50}$	-3.56	0.64
		$h$	1.09	0.85
		$I_{max}$	1.00	0.53
TNP-ATP	Kir6.2*-GFP+SUR1 n = 9	$IC_{50}$	-5.21	0.10
		$h$	0.92	0.18
		$I_{max}$	0.96	0.05
TNP-ATP	Kir6.2*-C166S-GFP+SUR1 n = 6	$IC_{50}$	-2.71	51.05
		$h$	1.14	15.79
		$I_{max}$	1.00	84.35
TNP-ATP	Kir6.2*-GFP+SUR-K205A n = 9	$IC_{50}$	-3.78	0.45
		$h$	0.75	0.30
		$I_{max}$	1.00	0.29
TNP-ATP	Kir6.2*-GFP+SUR-K205E n = 9	$IC_{50}$	-3.20	2.15
		$h$	0.79	0.84
		$I_{max}$	1.00	1.77
Fluorescence Quenching				
TNP-ATP	Kir6.2*-GFP+SUR1 n = 9	$EC_{50}$	-4.11	0.09
		$h$	0.87	0.11
		$E_{max}$	1.00	0.06
TNP-ATP	Kir6.2*-C166S-GFP+SUR1 n = 6	$EC_{50}$	-4.17	0.23
		$h$	0.84	0.27
		$E_{max}$	1.00	0.14
TNP-ATP	Kir6.2*-GFP+SUR-K205A n = 9	$EC_{50}$	-3.69	0.42
		$h$	0.73	0.25
		$E_{max}$	1.00	0.27
TNP-ATP	Kir6.2*-GFP+SUR-K205E n = 9	$EC_{50}$	-3.37	1.10
		$h$	0.74	0.47
		$E_{max}$	1.00	0.79

**Table 2. Table 2: Hill fit parameters from excised patches.**  $EC_{50}$  values and their standard errors are reported in  $\log_{10} M^{-1}$ .

Full MWC Construct	Term	Estimate	2.5% Quantile	97.5% Quantile
Kir6.2*-GFP+SUR1 n = 9	$L$	-1.05	-1.85	-0.45
	$D$	0.04	0.00	0.19
	$K_A$	4.32	4.21	4.44
Kir6.2*-C166S-GFP+SUR1 n = 6	$L$	0.29	-1.04	1.41
	$D$	0.84	0.52	0.95
	$K_A$	4.18	3.93	4.47
Kir6.2*-GFP+SUR-K205A n = 9	$L$	-0.37	-1.34	0.41
	$D$	0.55	0.39	0.65
	$K_A$	3.76	3.59	3.95
Kir6.2*-GFP+SUR-K205E n = 9	$L$	-0.18	-1.25	0.70
	$D$	0.62	0.42	0.74
	$K_A$	3.40	3.21	3.62
<b>Single-site</b>				
Kir6.2*-GFP+SUR1 n = 9	$L$	-1.06	-1.84	-0.47
	$D$	0.05	0.01	0.10
	$K_A$	4.33	4.22	4.44
Kir6.2*-C166S-GFP+SUR1 n = 6	$L$	0.09	-1.15	1.05
	$D$	0.70	0.29	0.91
	$K_A$	4.15	3.88	4.43
Kir6.2*-GFP+SUR-K205A n = 9	$L$	-0.25	-1.30	0.53
	$D$	0.18	0.06	0.32
	$K_A$	3.62	3.45	3.83
Kir6.2*-GFP+SUR-K205E n = 9	$L$	-0.19	-1.19	0.52
	$D$	0.30	0.13	0.47
	$K_A$	3.31	3.13	3.50
<b>Negative cooperativity</b>				
Kir6.2*-GFP+SUR1 n = 9	$L$	-0.42	-1.38	0.48
	$D$	0.15	0.02	0.29
	$K_A$	4.82	4.54	5.29
	$C$	0.17	0.06	0.36
Kir6.2*-C166S-GFP+SUR1 n = 6	$L$	0.32	-0.96	1.47
	$D$	0.83	0.50	0.94
	$K_A$	4.43	4.04	5.14
	$C$	0.52	0.09	0.97
Kir6.2*-GFP+SUR-K205A n = 9	$L$	-0.16	-1.18	0.64
	$D$	0.52	0.32	0.64
	$K_A$	4.10	3.73	4.68
	$C$	0.35	0.10	0.91
Kir6.2*-GFP+SUR-K205E n = 9	$L$	0.03	-1.11	0.99
	$D$	0.58	0.32	0.73
	$K_A$	3.71	3.34	4.41
	$C$	0.45	0.10	0.96

**Table 3. Table 3: Fitted parameters for the MWC-type models.**  $L$ ,  $K_A$  and their associated quantiles are reported as  $\log_{10}$  values to maintain consistency of the accuracy they are reported at.

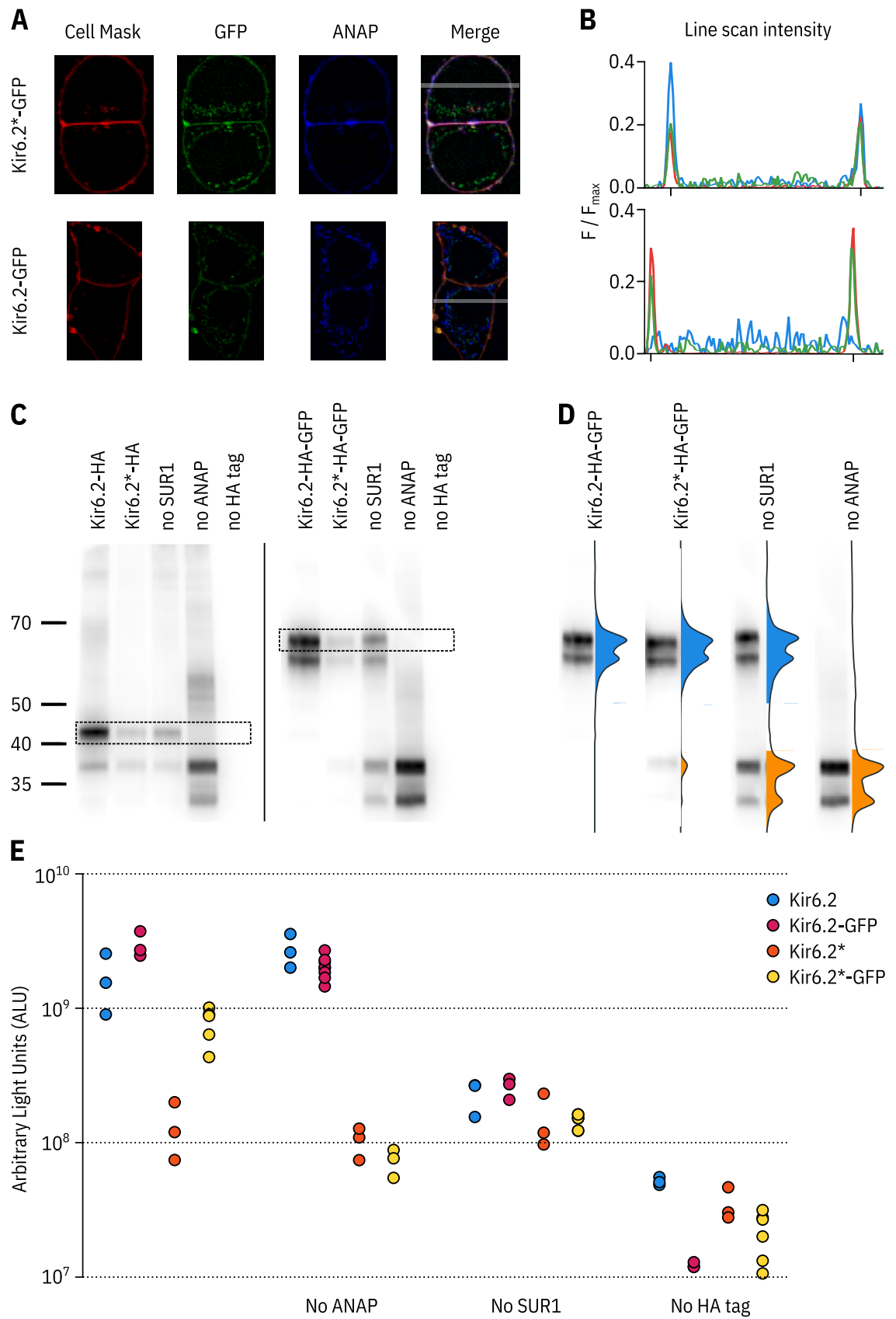
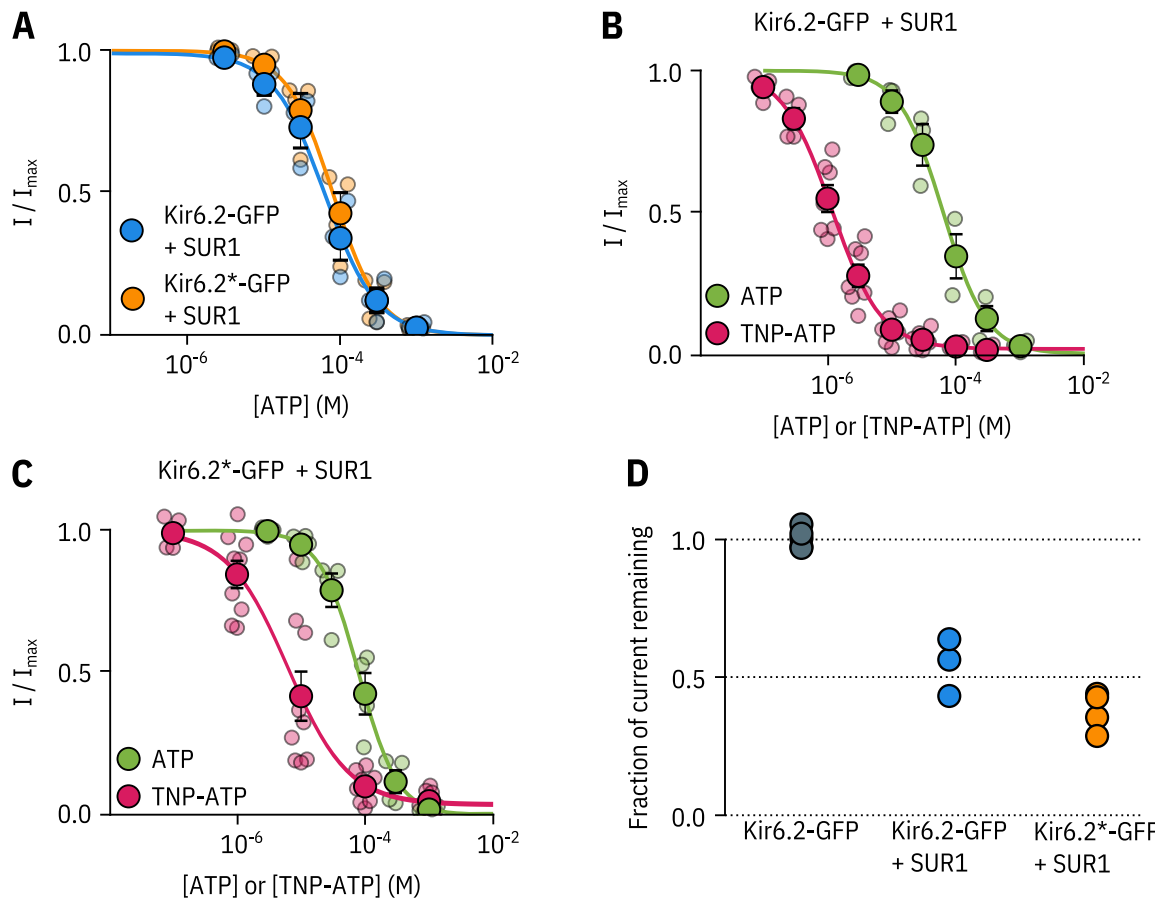
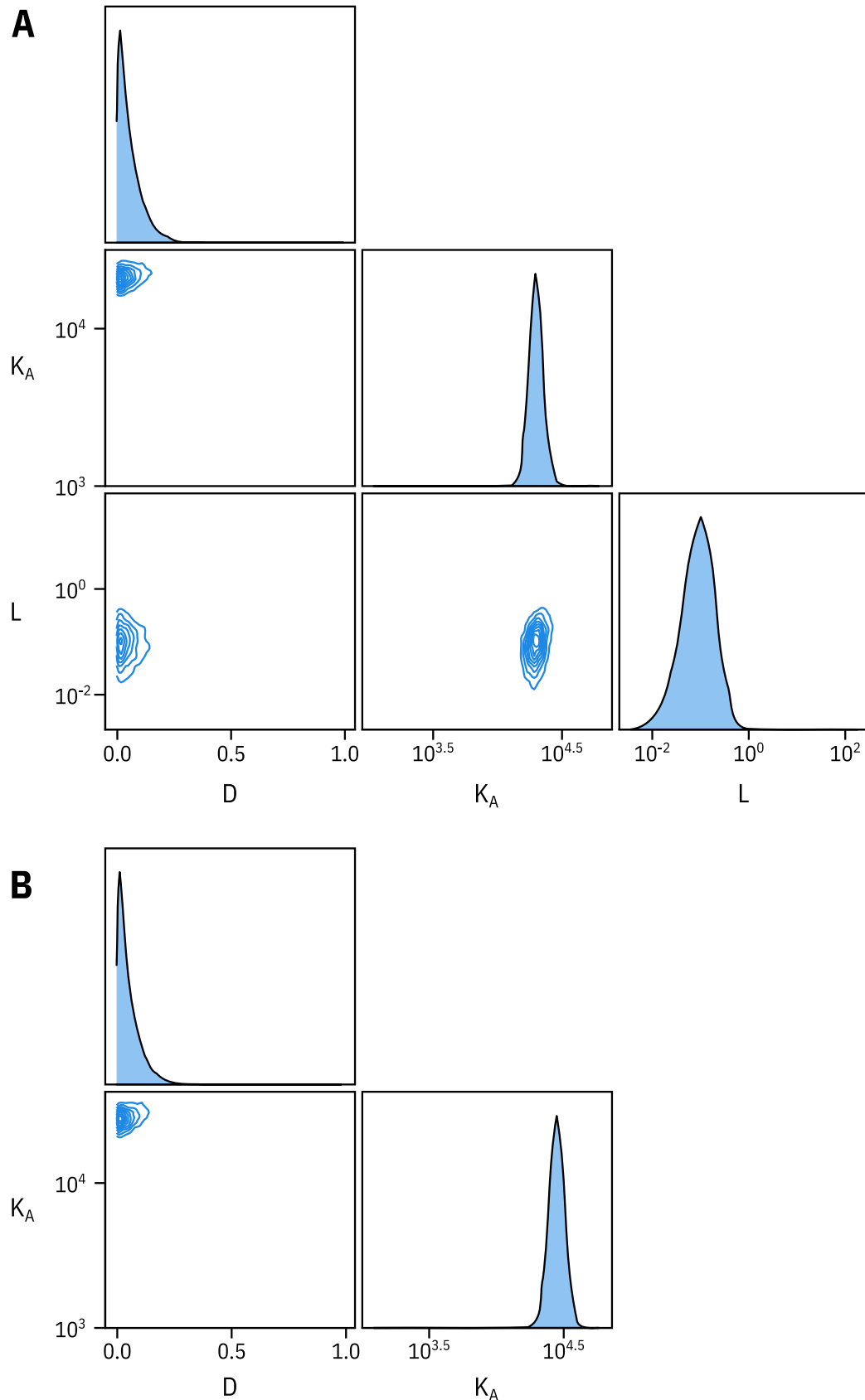


Figure 1 – figure supplement 1. ANAP labelling is specific and only full-length Kir6.2 is expressed at the cell membrane.

**Figure 1 – figure supplement 1. ANAP labelling is specific and only full-length Kir6.2 is expressed at the cell membrane.** **A.** Confocal images of HEK-293T cells transfected with Kir6.2\*-GFP + SUR1 (top panel) or Kir6.2-GFP + SUR1 (bottom panel). Cells were stained with Cell Mask Deep Red to label the plasma membrane. The grey band in the merged image is a 5-pixel width line scan. **B.** Averaged intensities of the line scans shown in **A**. The intensity of each channel is shown as a differently coloured line: Cell Mask in red, ANAP in blue and GFP in green. The notches on the x-axis mark the location of the plasma membrane. **C.** Two separate western blots against Kir6.2\*-HA (left) and Kir6.2\*-HA-GFP (right) constructs. Cells were co-transfected with pANAP, eRF1-E55D, and SUR1 unless otherwise indicated. Full-length Kir6.2 constructs are indicated on each gel with a dashed box. **D.** Each lane from the Kir6.2\*-HA-GFP gel is displayed normalised to its highest intensity accompanied by the line averaged density trace. The density peak corresponding to ANAP-labelled Kir6.2 is filled in blue. The density peak for C-terminally truncated Kir6.2 is filled in orange. **E.** Chemiluminescence-based surface expression assay for Kir6.2-HA constructs. Each data point represents an individual coverslip of transfected HEK-293T cells. n = 3-6 for each condition. Note the logarithmic scale on the vertical axis.



**Figure 1 – figure supplement 2. Kir6.2\*-GFP is functionally similar to Kir6.2-GFP.** **A.** Concentration-response curve for ATP inhibition of Kir6.2-GFP + SUR1 or Kir6.2\*-GFP + SUR1, measured in excised, inside-out patches. The smooth curves are descriptive Hill fits to the data. Kir6.2-GFP + SUR1:  $IC_{50} = 62.7 \mu\text{M}$ ,  $h = 1.28$ ,  $I_{max} = 0.99$ ,  $n = 3$ ; Kir6.2\*-GFP + SUR1:  $IC_{50} = 79.5 \mu\text{M}$ ,  $h = 1.42$ ,  $I_{max} = 1.00$ ,  $n = 4$ . **B, C.** Concentration-response relationships for current inhibition in excised, inside-out patches expressing Kir6.2-GFP + SUR1 (**C**) or Kir6.2\*-GFP + SUR1 (**D**) exposed to either ATP or TNP-ATP. The smooth curves are descriptive Hill fits to the data. Kir6.2-GFP + SUR1 (TNP-ATP):  $IC_{50} = 1.17 \mu\text{M}$ ,  $h = 1.14$ ,  $I_{max} = 0.97$ ,  $n = 7$ , Kir6.2\*-GFP + SUR1 (TNP-ATP):  $IC_{50} = 6.23 \mu\text{M}$ ,  $h = 0.92$ ,  $I_{max} = 0.96$ ,  $n = 9$ . Data and fits for inhibition of Kir6.2\*-GFP + SUR1 by TNP-ATP are the same as in Figure 2. **D.** Fractional current inhibition by 100  $\mu\text{M}$  tolbutamide measured in excised, inside out patches. Data were normalised to the average current in control solution before and after tolbutamide exposure. Each data point represents an individual patch. Kir6.2-GFP without SUR1,  $n = 5$ ; Kir6.2-GFP + SUR1,  $n = 3$ ; Kir6.2\*-GFP + SUR1,  $n = 4$ .



**Figure 2 – figure supplement 1. Fixing  $L$  does not affect estimates of  $D$  and  $K_A$ .** **A.** Pairwise correlation plots of  $L$ ,  $D$  and  $K_A$  from the full MWC-type model fit to Kir6.2\*-GFP + SUR1. **B.** Pairwise correlation plots of  $D$  and  $K_A$  from the full MWC-type with  $L$  fixed to 0.8 ( $P_{open} = 0.45$ ).

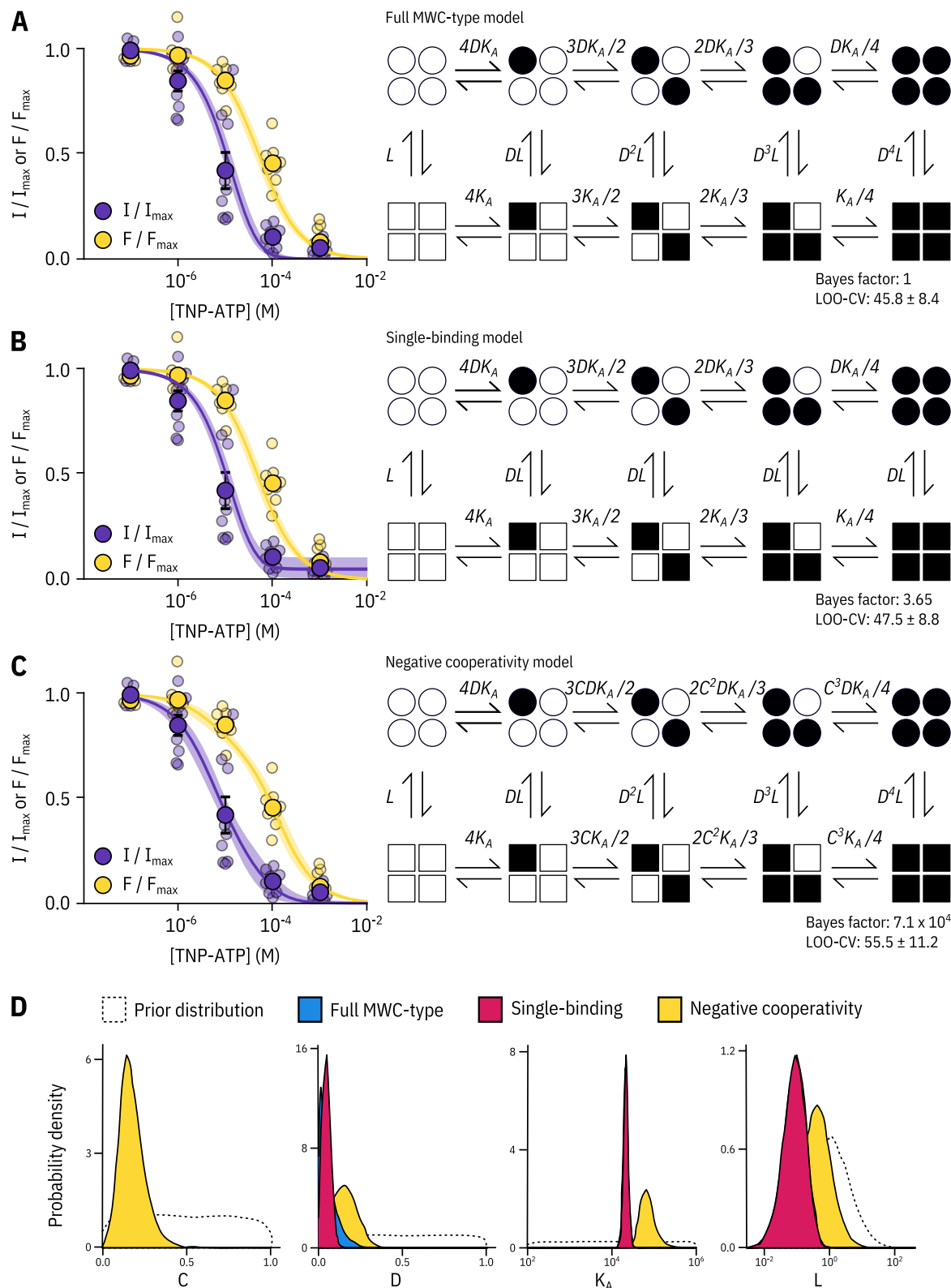


**Figure 2 – figure supplement 2. Model selection.** Fits to PCF data from Figure 2 with the full MWC-type model (**A**), single-binding model (**B**) and negative-cooperativity model (**C**) are shown on the left with the diagrammatic formulation of each model on the right. The Bayes factor and leave-one-out cross-validation (LOO-CV) scores for each model compared to the full MWC-type model are displayed.  $L$ ,  $D$ ,  $C$ , and  $K_A$  are defined in the text. **D**. Posterior probability distributions for the each of the models generated by MCMC fits to the data in Figure 2 overlaid on the prior probability distribution (dashed line) for each parameter. For  $L$  and  $K_A$ , the distributions for the MWC-type and single-binding model were virtually identical. The MWC-type densities are hidden behind the single-binding densities.

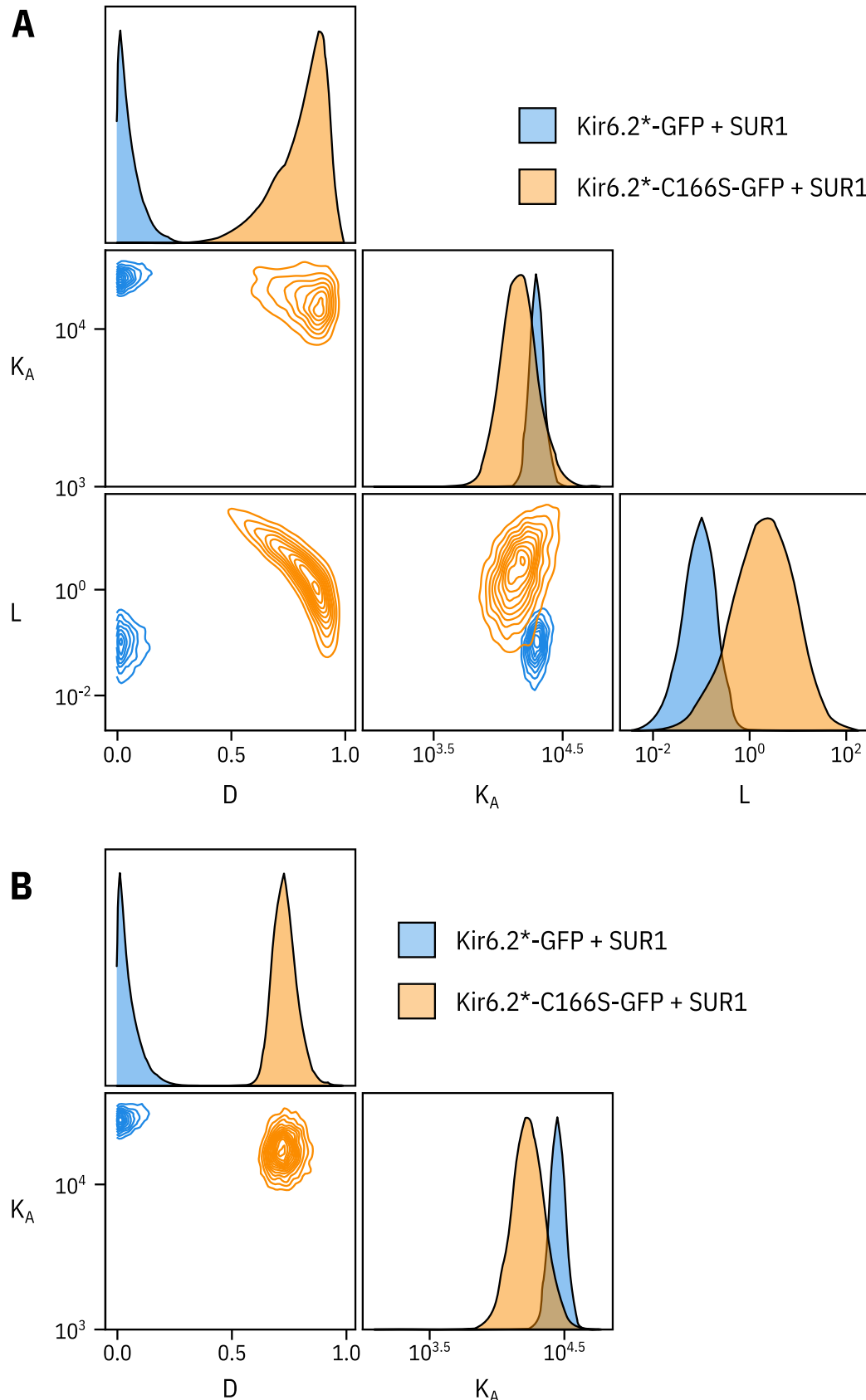


**Figure 3 – figure supplement 1. Fixing  $L$  does not affect the other two parameters.** **A.** Pairwise correlation plots of  $L$ ,  $D$  and  $K_A$  from the full MWC-type model fit to Kir6.2\*-GFP + SUR1 and Kir6.2\*-C166S-GFP + SUR1. **B.** Pairwise correlation plots of  $D$  and  $K_A$  from the full MWC-type model fit to Kir6.2\*-GFP + SUR1 ( $P_{open} = 0.45$ ) or 6.0 for Kir6.2\*-C166S-GFP + SUR1 ( $P_{open} = 0.86$ ).

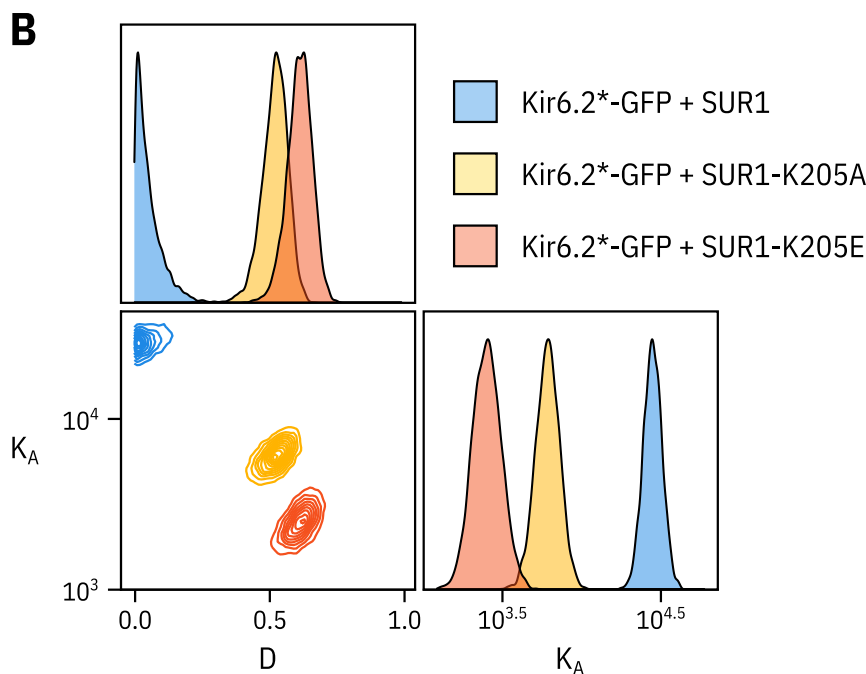
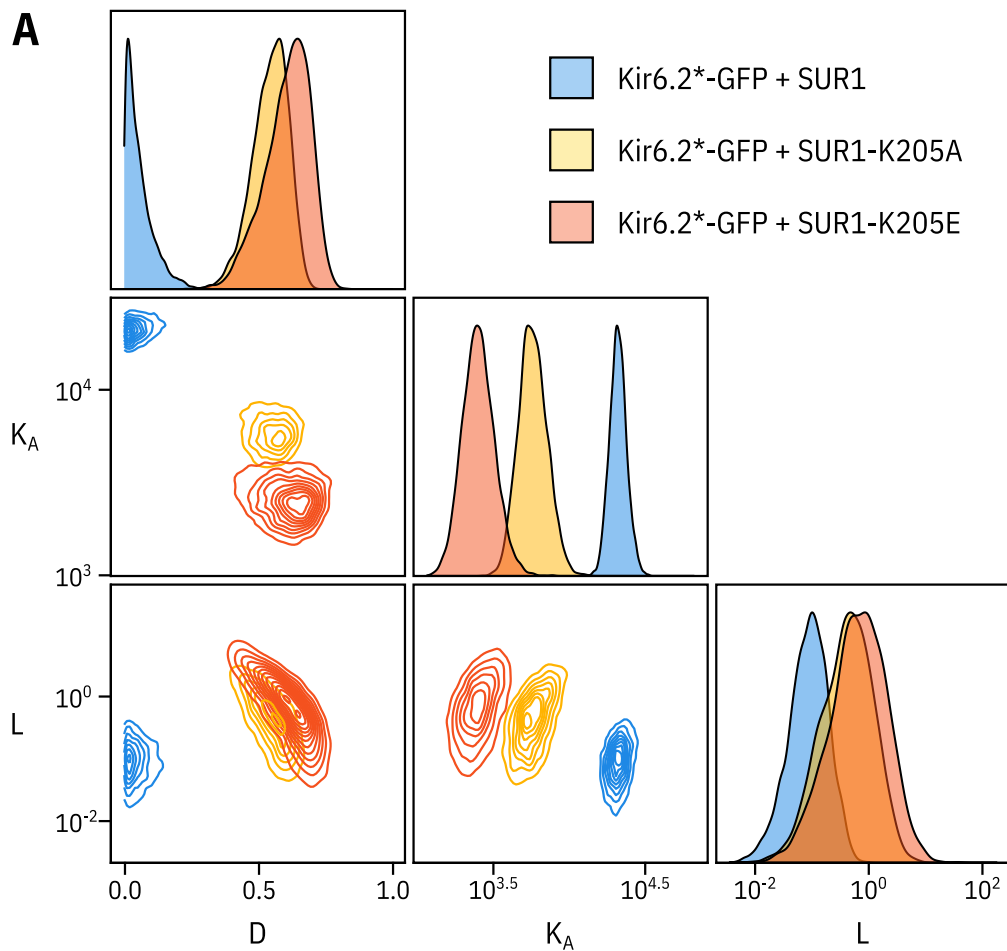


**Figure 5 – figure supplement 1. Fixing the  $L$  parameter does not drastically affect the fits to the SUR1-K205A or SUR1-K205E data.** **A.** Pairwise correlation plots of  $L$ ,  $D$  and  $K_A$  from the full MWC-type model fit to Kir6.2\*-GFP co-expressed with wild-type SUR1, SUR1-K205A, and SUR1-K205E. **B.** Pairwise correlation plots of  $D$  and  $K_A$  from the full MWC-type as above with  $L$  fixed to 0.8 (Trapp et al., 1998).

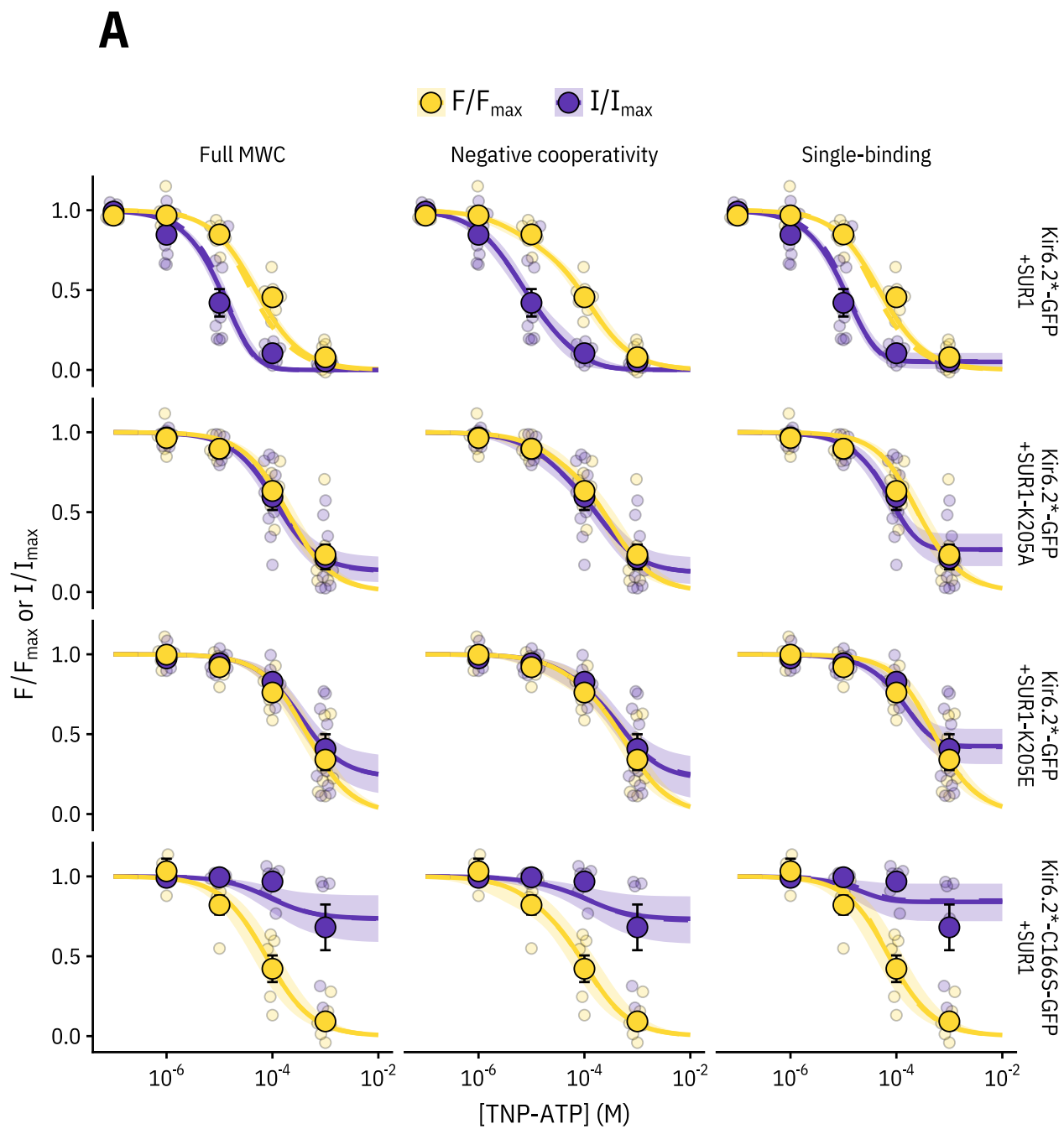


**Figure 5 – figure supplement 1. Comparing the ability of each model to explain the data.** Fits for each construct with each model (MWC-type, single-binding, negative-cooperativity) are displayed with the solid curve representing the median fit, the shaded area representing the 95% quartiles, and the dashed curve representing the median fit if the  $L$  parameter is fixed (to 6.0 for  $\text{Kir6.2}^*-\text{C166S}-\text{GFP} + \text{SUR1}$  and to 0.8 for the other three constructs). As the two fits were very similar, the dashed curve mostly overlays the solid curve. The most notable differences between the fits are that the negative cooperativity model allows for non-sigmoidal curves, and the single-binding model predicts much larger pedestals of current at saturating concentrations of TNP-ATP than either of the other two models.